


Optical deformation of homogeneous and core-shell spherical particles

Benjamin Vennes and Thomas C. Preston ^{*}

*Department of Atmospheric and Oceanic Sciences and Department of Chemistry,
McGill University, 805 Sherbrooke Street West, Montreal, Quebec H3A 0B9*



(Received 11 February 2020; accepted 11 May 2020; published 5 June 2020)

We study the optical stress and deformation of a dielectric sphere by an arbitrary shaped electromagnetic beam. The incident optical beam is described within the framework of generalized Lorenz-Mie theory (GLMT). A model based on the stress balance across a static fluid interface is used to determine the optical deformation of a particle composed of concentric spherical shells. An important analytic expression for the optical deformation is derived. With this result, we examine the optical stress and deformation of (i) a homogeneous spherical particle and (ii) a sphere with a concentric spherical shell. Illumination by both linearly and circularly polarized Gaussian and zeroth-order Bessel beams are considered. Cases relevant to optical trapping and manipulation experiments are analyzed.

DOI: [10.1103/PhysRevA.101.063812](https://doi.org/10.1103/PhysRevA.101.063812)

I. INTRODUCTION

The classic radiation pressure experiment of Ashkin and Dziedzic found that light entering or exiting a transparent liquid with a higher refractive index than its surroundings would result in an outward bulging of the liquid surface [1]. Subsequent analysis explained this observation as the result of optical forces parallel to the liquid surface that arise due to the tightly focused Gaussian beam used in the experiment rather than momentum transfer along the direction of beam propagation [2–4]. Spherical microdroplets have also been used as a platform for both experimental and theoretical investigations into both linear and nonlinear optical deformation [5–9]. For these experiments, models that build on Mie theory and utilize the Minkowski form of the Maxwell stress tensor have been able to accurately calculate radiation pressure and, subsequently, the observed deformation through the Navier-Stokes equation [6,7].

The phenomenon of radiation pressure is also at the heart of the optical manipulation of micron- and nanosized objects. From the initial demonstration of optical trapping [10] and levitation [11] to the invention of the optical tweezers [12] and the multitude of applications that have since followed, including dynamic holographic optical tweezers [13], single aerosol particle measurements [14], optical pulling [15], particle sorting [16], and single biomolecule studies [17]. Typically, the amount of deformation that occurs during optical trapping is negligible in these applications. For instance, even with liquid droplets, a micron-sized particle will be deformed by less than one nanometer when held using normal trapping powers [18] and the amount of deformation for a solid particle would be even less than that. However, ultralow interfacial tensions (on the order of 10^{-3} mN/m) [19] can be achieved in, for instance, water-in-oil reverse micelles, resulting in large deformations that are observable at typical trapping powers

[20,21]. The so-called optical stretcher consists of two co-axial counterpropagating beams and has been used to measure the viscoelastic properties of soft biological materials (e.g., soft cells) [22,23].

In atmospheric science, surface tension has long been known to play a key role in cloud droplet activation [24] and, more recently, changing surface tension has also been identified as being of great importance during the cloud droplet formation process [25–27]. Liquid-liquid phase separation can occur in atmospheric aerosol particles [28,29] and result in a core-shell droplet with a lower surface tension than if it was homogeneously mixed [30]. The potential to study surface tension (along with interfacial tension at the core-shell interface in phase-separated particles) through optical deformation measurements of single microdroplets is appealing due to the relative humidity-controlled, contact-free environment that optical tweezers enable. Such a measurement is hindered by surface tensions well above the ultralow surface tension range (e.g., the surface tension of pure water is 73 mN/m at 20 °C) [31], so optical deformation of aqueous aerosols will not be observable using bright-field microscopy. However, weakly absorbing microdroplets can act as high-quality optical cavities that support whispering gallery modes (WGMs). By measuring the frequency splitting of WGMs that occurs when the spherical shape of a microdroplet undergoes a small change [32,33], deformations on the order of nanometers can be detected [34–36] and used to determine the surface tension of the droplet [18]. The development of a model that can be used to analyze such optical deformation measurements partially motivates the current work.

In this paper, we present a theoretical model to study the optical deformation of a particle composed of concentric spherical shells. In particular, we will focus our attention on (i) a homogeneous spherical particle and (ii) a homogeneous spherical particle with a homogeneous concentric spherical shell (referred to here as a core-shell particle). In Sec. II, we present the electromagnetic theory and generalized Lorenz-Mie theory (GLMT) formalism that is used to determine the

^{*}thomas.preston@mcgill.ca

optical stress of an arbitrarily shaped beam on a spherical surface or interface. In Sec. III, an analytic expression for the amplitude of deformation is derived by balancing the radiation pressure, hydrostatic pressure difference, and the product of tension and curvature across an interface or surface. This derivation is a key result of the current work. In Sec. IV, the expressions are used to study the optical stress and deformation of microdroplets with physically relevant parameters in several cases that are important to optical trapping and manipulation (particles illuminated by Gaussian or zeroth-order Bessel beams).

II. ELECTROMAGNETIC THEORY

A. Optical stress

In a medium that is both charge-free and nonmagnetic, the electromagnetic force density is the sum of the electrostrictive force, Minkowski's tensor, and Abraham's tensor [7,37]. Under steady-state conditions at optical frequencies, only the Minkowski tensor is required for accurate radiation pressure calculations, and the other two terms in the electromagnetic force expression can be ignored [8,38]. Therefore, the appropriate form of the Maxwell stress tensor \vec{T} for our calculations is

$$\vec{T} = \mathbf{E} \otimes \mathbf{D} + \mathbf{B} \otimes \mathbf{H} - \frac{1}{2} \vec{T} (\mathbf{E} \cdot \mathbf{D} + \mathbf{B} \cdot \mathbf{H}), \quad (1)$$

where the constitutive relations between the electric field \mathbf{E} and the magnetic field \mathbf{H} and the auxiliary fields \mathbf{D} and \mathbf{B} are $\mathbf{D} = \varepsilon \mathbf{E}$ and $\mathbf{B} = \mu \mathbf{H}$, respectively. The quantities ε and μ are the dielectric permittivity and magnetic permeability of the medium, respectively.

The time-averaged component of the stress tensor acting on the plane with a normal unit vector $\hat{\mathbf{e}}_r$ is

$$\begin{aligned} \langle \hat{\mathbf{e}}_r \cdot \vec{T} \rangle = \text{Re} \{ & \frac{1}{4} \hat{\mathbf{e}}_r [\varepsilon (E_r E_r^* - E_\theta E_\theta^* - E_\phi E_\phi^*) \\ & + \mu (H_r H_r^* - H_\theta H_\theta^* - H_\phi H_\phi^*) \\ & + \frac{1}{2} [\hat{\mathbf{e}}_\theta (\varepsilon E_r E_\theta^* + \mu H_r H_\theta^*) \\ & + \hat{\mathbf{e}}_\phi (\varepsilon E_r E_\phi^* + \mu H_r H_\phi^*)] \}. \end{aligned} \quad (2)$$

The radiation pressure $\sigma_j(\theta, \phi)$ on the j th interface located at $r = a_j$ is

$$\sigma_j(\theta, \phi) = \hat{\mathbf{e}}_r \cdot (\langle \hat{\mathbf{e}}_r \cdot \vec{T} \rangle_{r=a_j^+} - \langle \hat{\mathbf{e}}_r \cdot \vec{T} \rangle_{r=a_j^-}). \quad (3)$$

We are only interested in the case where ε changes across the interface (μ is the same everywhere). Therefore, in Eq. (3), all of the terms containing components of the field \mathbf{H} will cancel out and the terms with components of the field \mathbf{E} can be evaluated by applying the boundary conditions for dielectric interfaces. Specifically, that the normal component of \mathbf{D} and the tangential component of \mathbf{E} are continuous. For the core-shell system shown in Fig. 1, the radiation pressure at the core-shell interface ($j = 1$) is then

$$\begin{aligned} \sigma_1 = \frac{\varepsilon_0}{4} \text{Re} [& (|\varepsilon_1/\varepsilon_2|^2 \varepsilon_2 - \varepsilon_1) E_r^{(1)} E_r^{(1)*} \\ & + (\varepsilon_1 - \varepsilon_2) (E_\theta^{(1)} E_\theta^{(1)*} + E_\phi^{(1)} E_\phi^{(1)*})], \end{aligned} \quad (4)$$

where $E_r^{(1)}$, $E_\theta^{(1)}$, and $E_\phi^{(1)}$ are the components of the electric field in the core, ε_1 is the dielectric permittivity of the core,

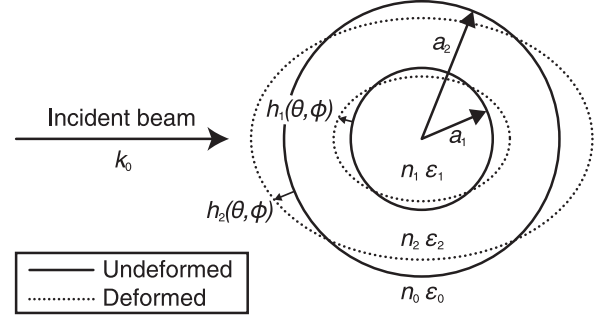


FIG. 1. Geometry of the undeformed and optically deformed core-shell particle.

and ε_2 is the dielectric permittivity of the shell. Similarly, the radiation pressure at the shell-medium interface ($j = 2$) is

$$\begin{aligned} \sigma_2 = \frac{\varepsilon_0}{4} \text{Re} [& (|\varepsilon_2/\varepsilon_0|^2 \varepsilon_0 - \varepsilon_2) E_r^{(2)} E_r^{(2)*} \\ & + (\varepsilon_2 - \varepsilon_0) (E_\theta^{(2)} E_\theta^{(2)*} + E_\phi^{(2)} E_\phi^{(2)*})], \end{aligned} \quad (5)$$

where $E_r^{(2)}$, $E_\theta^{(2)}$, and $E_\phi^{(2)}$ are the components of the electric field in the shell and ε_0 is the dielectric permittivity of the surrounding medium. Calculation of the fields for an arbitrary incident beam within the GLMT framework will now be discussed.

B. Field expansion in spherical vector wave functions

In GLMT, the electromagnetic field is expanded in the basis of spherical vector wave functions (SVWFs). For clarity, we will omit the harmonic time dependence $\exp(-i\omega t)$ from these expressions and throughout the rest of the text. Using SVWFs, the incident electric field is expanded as

$$\begin{aligned} \mathbf{E}^{\text{inc}}(\mathbf{r}) = E_0 \sum_{l=1}^{\infty} \sum_{m=-l}^l c_l^{pw} [& g_{lm}^{\text{TE}} \mathbf{M}_{lm}^{(1)}(k_0 r, \theta, \phi) \\ & - i g_{lm}^{\text{TM}} \mathbf{N}_{lm}^{(1)}(k_0 r, \theta, \phi)], \end{aligned} \quad (6)$$

where E_0 is the complex amplitude of the incident electric field, k_0 is the wave number in the medium, $c_l^{pw} = i^l (2l+1)/l(l+1)$ is the plane wave coefficient, g_{lm}^{TE} and g_{lm}^{TM} are the beam-shape coefficients (BSCs) for transverse electric (TE) and transverse magnetic (TM) polarization, respectively. The SVWFs $\mathbf{M}_{lm}^{(\alpha)}$ and $\mathbf{N}_{lm}^{(\alpha)}$ are expressed as [39]

$$\begin{aligned} \mathbf{M}_{lm}^{(\alpha)} = [& im\pi_l^{|m|} (\cos \theta) \hat{\mathbf{e}}_\theta - \tau_l^{|m|} (\cos \theta) \hat{\mathbf{e}}_\phi] z_l^{(\alpha)}(kr) e^{im\phi}, \quad (7) \\ \mathbf{N}_{lm}^{(\alpha)} = \left\{ & l(l+1) P_l^{|m|}(\cos \theta) \frac{z_l^{(\alpha)}(kr)}{kr} \hat{\mathbf{e}}_r + [\tau_l^{|m|}(\cos \theta) \hat{\mathbf{e}}_\theta \right. \\ & \left. + im\pi_l^{|m|}(\cos \theta) \hat{\mathbf{e}}_\phi] \frac{[kr z_l^{(\alpha)}(kr)]'}{kr} \right\} e^{im\phi}, \end{aligned} \quad (8)$$

where the function $z_l^{(\alpha)}$ is the l th-order spherical Bessel function of the first kind $z_l^{(1)} = j_l$, second kind $z_l^{(2)} = y_l$, or the spherical Hankel function $z_l^{(3)} = h_l^{(1)}$. Note that the primes in Eq. (8) indicate differentiation with respect to the argument.

The angular functions in Eqs. (7) and (8) are

$$\begin{aligned}\pi_l^{||m|}(\cos\theta) &= \frac{P_l^{||m|}(\cos\theta)}{\sin\theta}, \\ \tau_l^{||m|}(\cos\theta) &= \frac{d}{d\theta}P_l^{||m|}(\cos\theta),\end{aligned}\quad (9)$$

and $P_l^{||m|}(\cos\theta)$ is the associated Legendre polynomial, defined without the $(-1)^m$ factor,

$$P_l^m(\cos\theta) = \sin\theta^m \frac{d^m}{d\cos\theta^m} P_l(\cos\theta). \quad (10)$$

Here, m is the azimuthal mode number and $P_l(\cos\theta)$ is the Legendre polynomial.

The magnetic field is obtained by making use of $\nabla \times \mathbf{E} = i\omega\mathbf{B}$, the constitutive relation between \mathbf{B} and \mathbf{H} , and the following curl identities of the SVWFs:

$$\nabla \times \mathbf{M}_{lm}^{(\alpha)} = k\mathbf{N}_{lm}^{(\alpha)}, \quad (11)$$

$$\nabla \times \mathbf{N}_{lm}^{(\alpha)} = k\mathbf{M}_{lm}^{(\alpha)}, \quad (12)$$

so that

$$\begin{aligned}Z_0\mathbf{H}^{\text{inc}}(\mathbf{r}) &= -E_0 \sum_{l=1}^{\infty} \sum_{m=-l}^l c_l^{pw} [g_{lm}^{\text{TM}}\mathbf{M}_{lm}^{(1)}(k_0r, \theta, \phi) \\ &\quad + ig_{lm}^{\text{TE}}\mathbf{N}_{lm}^{(1)}(k_0r, \theta, \phi)],\end{aligned}\quad (13)$$

where $Z_0 = \sqrt{\mu_0/\varepsilon_0}$ is the impedance in the surrounding medium. By exploiting the orthogonality of $P_l^{||m|}(\cos\theta)\exp(im\phi)$, the BSCs can be expressed in terms of the radial component of the incident beam

$$\begin{aligned}g_{lm}^{\text{TM}} &= \frac{(-i)^{l-1}}{4\pi E_0} \frac{k_0r}{j_l(k_0r)} \frac{(l-|m|)!}{(l+|m|)!} \int_0^{2\pi} \int_0^\pi \sin\theta d\theta \\ &\quad \times d\phi(\mathbf{E}^{\text{inc}} \cdot \hat{\mathbf{e}}_r) P_l^{||m|}(\cos\theta) e^{-im\phi},\end{aligned}\quad (14)$$

$$\begin{aligned}g_{lm}^{\text{TE}} &= \frac{(-i)^{l-1}}{4\pi E_0} \frac{k_0r}{j_l(k_0r)} \frac{(l-|m|)!}{(l+|m|)!} \int_0^{2\pi} \int_0^\pi \sin\theta d\theta \\ &\quad \times d\phi(Z_0\mathbf{H}^{\text{inc}} \cdot \hat{\mathbf{e}}_r) P_l^{||m|}(\cos\theta) e^{-im\phi}.\end{aligned}\quad (15)$$

In this work, we will investigate both linearly and circularly polarized Gaussian and Bessel beams that are incident upon a spherical particle. For a linearly polarized Gaussian beam, an analytical form of the BSCs can be found using the localized approximation (see Appendix A) [40]. For the zeroth-order Bessel beam, analytic expressions for the BSCs in the framework of the GLMT are given in Appendix B [41]. The BSCs for a circularly polarized beam can be determined using the BSCs for a linearly polarized beam and the relationships [42]

$$g_{lm}^{\text{TM},\pm} = \frac{1}{\sqrt{2}}(g_{lm}^{\text{TM}} \pm ig_{lm}^{\text{TE}}), \quad g_{lm}^{\text{TE},\pm} = \frac{1}{\sqrt{2}}(g_{lm}^{\text{TE}} \mp ig_{lm}^{\text{TM}}), \quad (16)$$

where $+$ ($-$) denotes right-hand (left-hand) circular polarization. Note that the time convention in Ref. [42] is $\exp(i\omega t)$, which differs from our choice of $\exp(-i\omega t)$ such that the results in Eq. (16) are not identical to the relations in that work.

The scattered fields are expanded as follows:

$$\begin{aligned}\mathbf{E}^{\text{sca}}(\mathbf{r}) &= E_0 \sum_{l=1}^{\infty} \sum_{m=-l}^l c_l^{pw} [ia_{lm}\mathbf{N}_{lm}^{(3)}(k_0r, \theta, \phi) \\ &\quad - b_{lm}\mathbf{M}_{lm}^{(3)}(k_0r, \theta, \phi)],\end{aligned}\quad (17)$$

$$\begin{aligned}Z_0\mathbf{H}^{\text{sca}}(\mathbf{r}) &= E_0 \sum_{l=1}^{\infty} \sum_{m=-l}^l c_l^{pw} [ib_{lm}\mathbf{N}_{lm}^{(3)}(k_0r, \theta, \phi) \\ &\quad + a_{lm}\mathbf{M}_{lm}^{(3)}(k_0r, \theta, \phi)],\end{aligned}\quad (18)$$

where the scattering coefficients a_{lm} and b_{lm} are to be determined by imposing boundary conditions on the surface.

For a core-shell particle (Fig. 1), the internal fields in the shell will be

$$\begin{aligned}\mathbf{E}^{(2)}(\mathbf{r}) &= E_0 \sum_{l=1}^{\infty} \sum_{m=-l}^l c_l^{pw} [d_{lm}^{(2)}\mathbf{M}_{lm}^{(1)}(k_2r, \theta, \phi) \\ &\quad - ic_{lm}^{(2)}\mathbf{N}_{lm}^{(1)}(k_2r, \theta, \phi) \\ &\quad + ie_{lm}^{(2)}\mathbf{N}_{lm}^{(2)}(k_2r, \theta, \phi) - f_{lm}^{(2)}\mathbf{M}_{lm}^{(2)}(k_2r, \theta, \phi)],\end{aligned}\quad (19)$$

$$\begin{aligned}Z_2\mathbf{H}^{(2)}(\mathbf{r}) &= -E_0 \sum_{l=1}^{\infty} \sum_{m=-l}^l c_l^{pw} [c_{lm}^{(2)}\mathbf{M}_{lm}^{(1)}(k_2r, \theta, \phi) \\ &\quad + id_{lm}^{(2)}\mathbf{N}_{lm}^{(1)}(k_2r, \theta, \phi) \\ &\quad - if_{lm}^{(2)}\mathbf{N}_{lm}^{(2)}(k_2r, \theta, \phi) - e_{lm}^{(2)}\mathbf{M}_{lm}^{(2)}(k_2r, \theta, \phi)],\end{aligned}\quad (20)$$

where Z_2 is the impedance in the shell and k_2 is the wave number in the shell. The latter is related to the wave number in the surrounding medium by $k_2 = n_2k_0$, where n_2 denotes the relative refractive index of the shell. Because of the singular nature of the Bessel function of the second kind y_l at the origin, the field expansion inside the core must have $e_{lm}^{(1)} = 0$ and $f_{lm}^{(1)} = 0$:

$$\begin{aligned}\mathbf{E}^{(1)}(\mathbf{r}) &= E_0 \sum_{l=1}^{\infty} \sum_{m=-l}^l c_l^{pw} [d_{lm}^{(1)}\mathbf{M}_{lm}^{(1)}(k_1r, \theta, \phi) \\ &\quad - ic_{lm}^{(1)}\mathbf{N}_{lm}^{(1)}(k_1r, \theta, \phi)],\end{aligned}\quad (21)$$

$$\begin{aligned}Z_1\mathbf{H}^{(1)}(\mathbf{r}) &= -E_0 \sum_{l=1}^{\infty} \sum_{m=-l}^l c_l^{pw} [c_{lm}^{(1)}\mathbf{M}_{lm}^{(1)}(k_1r, \theta, \phi) \\ &\quad + id_{lm}^{(1)}\mathbf{N}_{lm}^{(1)}(k_1r, \theta, \phi)].\end{aligned}\quad (22)$$

$k_1 = n_1k_0$ denotes the wave number in the core with relative refractive index n_1 . The internal coefficients are determined from the boundary conditions on the core-shell interface.

III. OPTICAL DEFORMATION

A. Interfacial stress balance and resulting deformation amplitude

The stress-balance equation for the j th interface can be found by incorporating σ_j into the Young-Laplace equation

to yield

$$\gamma_j \nabla \cdot \hat{\mathbf{n}}_j = \Delta p_j + \sigma_j, \quad (23)$$

where γ_j is the interfacial or surface tension, $\hat{\mathbf{n}}_j$ is an outward unit vector normal to the interface, and $\Delta p_j = p_j^{\text{in}} - p_j^{\text{ext}}$ is the difference in fluid pressure across the interface. For a static fluid, the Navier-Stokes equation gives $\nabla p_j^{\text{in}} = 0$ and $\nabla p_j^{\text{ext}} = 0$ [7]. Then, the excess pressure induced by the Minkowski tensor has no angular dependence because p_j^{in} and p_j^{ext} are constant values. As such, Δp_j is a constant that varies according to the j th interface under consideration. The deformation at the j th interface will be defined as $h_j(\theta, \phi)$ and can be represented as an expansion using spherical harmonics

$$h_j(\theta, \phi) = \sum_{l=2}^{\infty} \sum_{m=-l}^l h_{lm}^{(j)} Y_{lm}(\theta, \phi), \quad (24)$$

where the spherical harmonics are defined as

$$Y_{lm}(\theta, \phi) = \begin{cases} \sqrt{\frac{(2l+1)(l-|m|)!}{4\pi(l+|m|)!}} P_l^{|m|}(\cos\theta) e^{im\phi} & \text{if } (m < 0), \\ (-1)^m \sqrt{\frac{(2l+1)(l-m)!}{4\pi(l+m)!}} P_l^m(\cos\theta) e^{im\phi} & \text{if } (m \geq 0). \end{cases} \quad (25)$$

The radial position of a deformed interface will be $d_j(\theta, \phi) = a_j + h_j(\theta, \phi)$. In Eq. (24), the $l = 0$ term is not included in the summation due to conservation of volume and the assumption that the fluid is incompressible and the $l = 1$ term is omitted as it corresponds to uniform motion [6].

For small deformations ($h_j \ll a_j$), the expansion [7]

$$\gamma_j \nabla \cdot \hat{\mathbf{n}}_j = \frac{2\gamma_j}{a_j} + \frac{\gamma_j}{a_j^2} \sum_{l=2}^{\infty} \sum_{m=-l}^l (l-1)(l+2) h_{lm}^{(j)} Y_{lm}(\theta, \phi) \quad (26)$$

can be inserted into Eq. (23) along with the following expansion in spherical harmonics for the radiation pressure

$$\sigma_j(\theta, \phi) = \sum_{l=1}^{\infty} \sum_{m=-l}^l \sigma_{lm}^{(j)} Y_{lm}(\theta, \phi). \quad (27)$$

Then, utilizing the orthogonality of the spherical harmonics, the deformation coefficients will be

$$h_{lm}^{(j)} = \frac{a_j^2}{\gamma_j} \frac{\sigma_{lm}^{(j)}}{(l-1)(l+2)}. \quad (28)$$

Although Eq. (28) relates the coefficients in a straightforward manner, the main difficulty is in first determining $\sigma_{lm}^{(j)}$. In the case of the core-shell system shown in Fig. 1, this would involve inserting either Eqs. (4) or (5) into the left-hand side (LHS) of Eq. (27) and using the orthogonality of the spherical harmonics to then solve for $\sigma_{lm}^{(j)}$. For the j th layer, this yields

$$\sigma_{lm}^{(j)} = \frac{2l+1}{8} \frac{(l-|m|)!}{(l+|m|)!} [(\varepsilon_j/\varepsilon_{j+1})^2 \varepsilon_{j+1} - \varepsilon_j] R_{lm}^{(j)} + (\varepsilon_j - \varepsilon_{j+1}) \Omega_{lm}^{(j)}, \quad (29)$$

where $R_{lm}^{(j)}$ and $\Omega_{lm}^{(j)}$ form the contribution of the radial and angular components of the electric field, respectively. They can be expressed by making use of either Eqs. (19) or (21) in expanding the internal field

$$R_{lm}^{(j)} = \frac{1}{2\pi} \sum_{l_1=1}^{\infty} \sum_{l_2=1}^{\infty} \sum_{m_1=-l_1}^{l_1} \sum_{m_2=-l_2}^{l_2} \int_0^{2\pi} \int_0^{\pi} \sin\theta d\theta d\phi \times E_r^{(j)} E_r^{(j)*} P_l^{|m|}(\cos\theta) e^{-im\phi}, \quad (30)$$

$$\Omega_{lm}^{(j)} = \frac{1}{2\pi} \sum_{l_1=1}^{\infty} \sum_{l_2=1}^{\infty} \sum_{m_1=-l_1}^{l_1} \sum_{m_2=-l_2}^{l_2} \int_0^{2\pi} \int_0^{\pi} \sin\theta d\theta d\phi \times [E_{\theta}^{(j)} E_{\theta}^{(j)*} + E_{\phi}^{(j)} E_{\phi}^{(j)*}] P_l^{|m|}(\cos\theta) e^{-im\phi}, \quad (31)$$

where it is understood that $E_r^{(j)}$, $E_{\theta}^{(j)}$, and $E_{\phi}^{(j)}$ are the internal electric field components that arise in the summand of either Eqs. (19) or (21). In what follows, the appropriate internal field components are inserted into Eqs. (30) and (31) and $R_{lm}^{(j)}$, $\Omega_{lm}^{(j)}$ are rewritten as

$$R_{lm}^{(j)} = \frac{|E_0|^2}{|k_j a_j|^4} A_{l_1 l_2 m_1 m_2}^{(j)} \mathcal{I}_{l_1 l_2 m_1 m_2}^A, \quad (32)$$

$$\Omega_{lm}^{(j)} = \frac{|E_0|^2}{|k_j a_j|^2} [B_{l_1 l_2 m_1 m_2}^{(j)} \mathcal{I}_{l_1 l_2 m_1 m_2}^B + C_{l_1 l_2 m_1 m_2}^{(j)} \mathcal{I}_{l_1 l_2 m_1 m_2}^C], \quad (33)$$

where l_{ij} and m_{ij} are shorthand for $l_i l_j$ and $m_i m_j$ respectively. Here, subscript indices that appear twice within a single term are implicitly summed over. All of the coefficients and terms that need to be evaluated on the surface but that do not depend on θ or ϕ are taken out of the surface integrals and regrouped into $A_{l_1 l_2 m_1 m_2}^{(j)}$, $B_{l_1 l_2 m_1 m_2}^{(j)}$, and $C_{l_1 l_2 m_1 m_2}^{(j)}$:

$$A_{l_1 l_2 m_1 m_2}^{(j)} = l_1(l_1+1)l_2(l_2+1)r_{l_1 m_1}^{(j)} r_{l_2 m_2}^{(j)*}, \quad (34)$$

$$B_{l_1 l_2 m_1 m_2}^{(j)} = [s_{l_1 m_1}^{(j)} s_{l_2 m_2}^{(j)*} + t_{l_1 m_1}^{(j)} t_{l_2 m_2}^{(j)*}], \quad (35)$$

$$C_{l_1 l_2 m_1 m_2}^{(j)} = [s_{l_1 m_1}^{(j)} t_{l_2 m_2}^{(j)*} + t_{l_1 m_1}^{(j)} s_{l_2 m_2}^{(j)*}], \quad (36)$$

with the terms $r_{lm}^{(j)}$, $s_{lm}^{(j)}$, and $t_{lm}^{(j)}$ given by

$$r_{lm}^{(j)} = c_l^{pw} [c_{lm}^{(j)} \psi_l(k_j a_j) + e_{lm}^{(j)} \chi_l(k_j a_j)], \quad (37)$$

$$s_{lm}^{(j)} = c_l^{pw} [c_{lm}^{(j)} \psi_l'(k_j a_j) + e_{lm}^{(j)} \chi_l'(k_j a_j)], \quad (38)$$

$$t_{lm}^{(j)} = c_l^{pw} [d_{lm}^{(j)} \psi_l(k_j a_j) + f_{lm}^{(j)} \chi_l(k_j a_j)]. \quad (39)$$

Here, we introduced the Riccati-Bessel functions ψ_l and χ_l which are related to the Bessel functions j_l and y_l through $\psi_l(\rho) = \rho j_l(\rho)$ and $\chi_l(\rho) = -\rho y_l(\rho)$.

$\mathcal{I}_{l_1 l_2 m_1 m_2}^A$, $\mathcal{I}_{l_1 l_2 m_1 m_2}^B$, and $\mathcal{I}_{l_1 l_2 m_1 m_2}^C$ are surface integrals that depend on θ and ϕ . They can be reduced to single integrals over θ by solving the ϕ integral first. The azimuthal integrals are straightforward to solve since they only involve products of complex exponentials [i.e., $\exp(im\phi)$]. The integration gives the condition that the azimuthal mode numbers are related by $m = m_1 - m_2$. If this condition is not met, the three integrals vanish. This will be implicit from now on. We then have the following:

$$\mathcal{I}_{l_1 l_2 m_1 m_2}^A = \int_0^{\pi} \sin\theta d\theta P_{l_1}^{|m_1|} P_{l_2}^{|m_2|} P_l^{|m|}, \quad (40)$$

$$\mathcal{I}_{l_1 l_2 m_1 l_2 m}^B = \int_0^\pi \sin \theta d\theta [m_1 m_2 \pi_{l_1}^{|m_1|} \pi_{l_2}^{|m_2|} + \tau_{l_1}^{|m_1|} \tau_{l_2}^{|m_2|}] P_l^{|m|}, \quad (41)$$

$$\mathcal{I}_{l_1 l_2 m_1 l_2 m}^C = - \int_0^\pi \sin \theta d\theta [m_1 \pi_{l_1}^{|m_1|} \tau_{l_2}^{|m_2|} + m_2 \tau_{l_1}^{|m_1|} \pi_{l_2}^{|m_2|}] P_l^{|m|}. \quad (42)$$

The resulting integrals contain triple products of $P_l^{|m|}$, $\pi_l^{|m|}$, and $\tau_l^{|m|}$ and these are not trivial to solve numerically due to the presence of numerous zeros on the domain of integration. Indeed, as l and m increase, the size of the subinterval must be decreased because the integrand contains functions that fluctuate rapidly with θ . This makes numerical inte-

gration computationally expensive and time-consuming. In Appendix C, exact expressions for the three integrals are given allowing us to derive an analytic expression for $\sigma_{lm}^{(j)}$. This will lead to the exact calculation of $h_j(\theta, \phi)$. The final result is subsequently summarized.

B. Summary and analytic expression for the optical deformation

The solutions to the three integrals are expressed in terms of the Wigner $3j$ symbols. These can be computed directly from Racah's formula [see Eqs. (C11) and (C12)] or by means of the recursion relations of the $3j$ symbols [43,44]. The first integral in question is given by

$$\mathcal{I}_{l_1 l_2 m_1 l_2 m}^A = 2(-1)^\Lambda \sqrt{\frac{(l_1 + |m_1|)!(l_2 + |m_2|)!(l + |m|)!}{(l_1 - |m_1|)!(l_2 - |m_2|)!(l - |m|)!}} \begin{pmatrix} l_1 & l_2 & l_3 \\ 0 & 0 & 0 \end{pmatrix} \begin{pmatrix} l_1 & l_2 & l \\ m_1 & -m_2 & -m \end{pmatrix}, \quad (43)$$

with $\Lambda = m_1 + \sum_{m_i < 0} m_i$. It is then shown that the second integral is actually related to the first one through

$$\mathcal{I}_{l_1 l_2 m_1 l_2 m}^B = \frac{1}{2} [l_1(l_1 + 1) + l_2(l_2 + 1) - l(l + 1)] \mathcal{I}_{l_1 l_2 m_1 l_2 m}^A. \quad (44)$$

The third integral is the most problematic, and is expressed by a finite series

$$\mathcal{I}_{l_1 l_2 m_1 l_2 m}^C = (-1)^\Lambda \sqrt{\frac{(l_1 + |m_1|)!(l_2 + |m_2|)!(l + |m|)!}{(l_1 - |m_1|)!(l_2 - |m_2|)!(l - |m|)!}} \times \left(m_1 \sum_{l_i=|l_1-l|}^{l_1+l} G_i \sqrt{\frac{(l_2 - |m_2|)!(l_i - |m_2|)!}{(l_2 + |m_2|)!(l_i + |m_2|)!}} \mathcal{I}_{l_2 m_2}^D + m_2 \sum_{l_j=|l_2-l|}^{l_2+l} H_j \sqrt{\frac{(l_j - |m_1|)!(l_1 - |m_1|)!}{(l_j + |m_1|)!(l_1 + |m_1|)!}} \mathcal{I}_{l_1 m_1}^D \right), \quad (45)$$

with the following terms:

$$G_i = (2l_i + 1) \begin{pmatrix} l_1 & l_i & l \\ 0 & 0 & 0 \end{pmatrix} \begin{pmatrix} l_1 & l_i & l \\ m_1 & -m_2 & -m \end{pmatrix},$$

$$H_j = (2l_j + 1) \begin{pmatrix} l_j & l_2 & l \\ 0 & 0 & 0 \end{pmatrix} \begin{pmatrix} l_j & l_2 & l \\ m_1 & -m_2 & -m \end{pmatrix},$$

$$\mathcal{I}_{l_j m}^D = \delta_{0,m} - \frac{(l_i + |m|)!}{(l_i - |m|)!} \delta_{2p+1, l_j - l_i} + \frac{(l_j + |m|)!}{(l_j - |m|)!} \delta_{2p+1, l_i - l_j},$$

where $p = 0, 1, 2, \dots$ is a positive integer.

When $\mathcal{I}_{l_1 l_2 m_1 l_2 m}^A$, $\mathcal{I}_{l_1 l_2 m_1 l_2 m}^B$, and $\mathcal{I}_{l_1 l_2 m_1 l_2 m}^C$ are known, these are inserted into $R_{lm}^{(j)}$ and $\Omega_{lm}^{(j)}$. All that remains is to compute the coefficients $A_{l_1 l_2 m_1 l_2}^{(j)}$, $B_{l_1 l_2 m_1 l_2}^{(j)}$, and $C_{l_1 l_2 m_1 l_2}^{(j)}$. This is done by matching the boundary conditions for the electric and magnetic fields at each interface and then calculating the quantities $r_{lm}^{(j)}$, $s_{lm}^{(j)}$, and $t_{lm}^{(j)}$. Thereafter, $\sigma_{lm}^{(j)}$ is computed from Eq. (29) and $h_{lm}^{(j)}$ from Eq. (28). The optical deformation is then found by inserting these coefficients into Eq. (24).

IV. RESULTS AND DISCUSSION

A. Homogeneous spherical particle in a Gaussian beam

In Fig. 2, we examine the optical stress and resulting deformation on a homogeneous spherical particle with a radius $a = 5 \mu\text{m}$ centered on the focal point of a single

Gaussian beam or the shared focal point of two coaxial counterpropagating Gaussian beams. The particle has physical parameters corresponding to water, with a refractive index of $n = 1.33$ and a surface tension of $\gamma = 73 \text{ mN/m}$ [45,46]. Linearly and circularly polarized Gaussian beams of three different beam waists, w_0 , are considered. The polar plots in Fig. 2 are in the plane of $\phi = 0^\circ$. With decreasing beam waist, there is an increase in optical stress in both the forward ($\theta = 0^\circ$) and backward ($\theta = 180^\circ$) directions. As the beam power is the same for all of the calculations, a more focused beam will transfer more momentum to the particle. Therefore, the narrowest beam waist ($w_0 = 0.2a$) has both the largest optical stress and deformation. In addition to the difference in magnitude, the results for the beam with the narrowest waist are qualitatively distinct from the case where the beam waist is the same as the particle radius ($w_0 = a$) and the case where the beam waist is large compared to the particle radius ($w_0 = 5a$).

When comparing the optical stress to the deformation calculations in Fig. 2 (and subsequent figures), one striking difference between the two sets of calculations is the absence of the sharp oscillations on the deformation plots. Sharp oscillations are observed for many of the optical stress plots but not their corresponding deformation plots which are always much smoother in curvature. The origin of this effect can be understood by examining Eq. (28), which relates stress coefficients $\sigma_{lm}^{(1)}$ to deformation coefficients $h_{lm}^{(1)}$ with

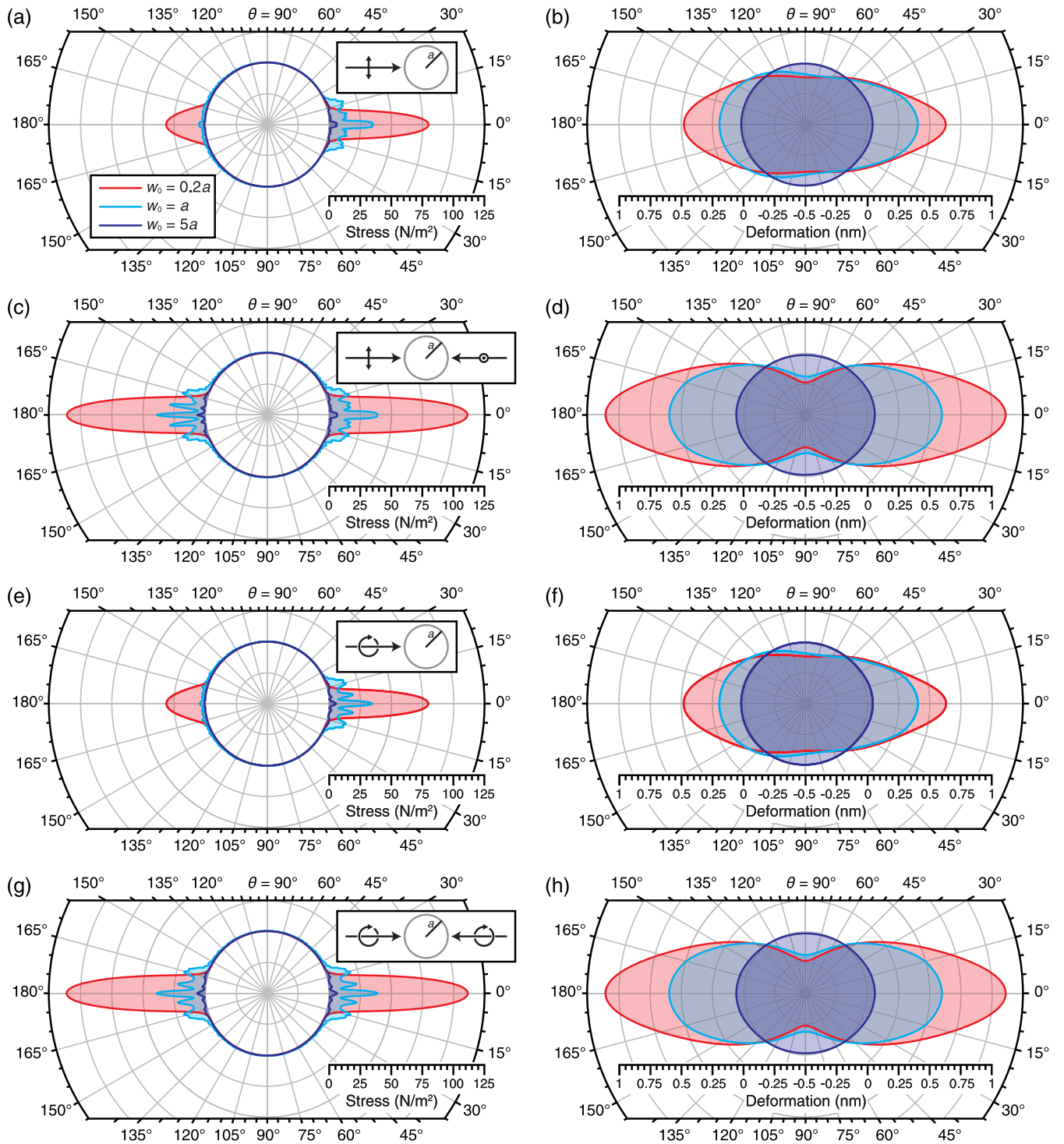


FIG. 2. The stress and deformation in the x - z plane induced by one or two Gaussian beams on a homogeneous sphere with a refractive index of $n = 1.33$, radius of $a = 5 \mu\text{m}$, and surface tension of $\gamma = 73 \text{ mN/m}$. The first row [(a), (b)] shows the case of an x polarized beam coming from $\theta = 180^\circ$. The second row [(c), (d)] shows the case of one x polarized beam coming from $\theta = 180^\circ$ and one y polarized beam coming from $\theta = 0^\circ$. The third and fourth rows [(e)–(h)] are the same as the first and second rows [(a)–(d)] except the polarization of the beam(s) is set to be left circular. In all cases, the beam waist of each Gaussian beam, w_0 , scales with the radius of the sphere while the beam power is held constant at $P = 0.1 \text{ W}$ and the beam wavelength is set to $\lambda = 0.532 \mu\text{m}$.

an extra factor of $(l - 1)(l + 2)$. This factor dampens the contribution of higher l spherical harmonics to the optical deformation calculated using Eq. (24). More generally, this is the result of curvature rather than deformation amplitude

being proportional to optical stress in the stress-balance equation [Eq. (23)].

In Figs. 2(a) and 2(e), the stress in the $\theta = 0^\circ$ direction is greatly enhanced due to the lensing of the light by the sphere

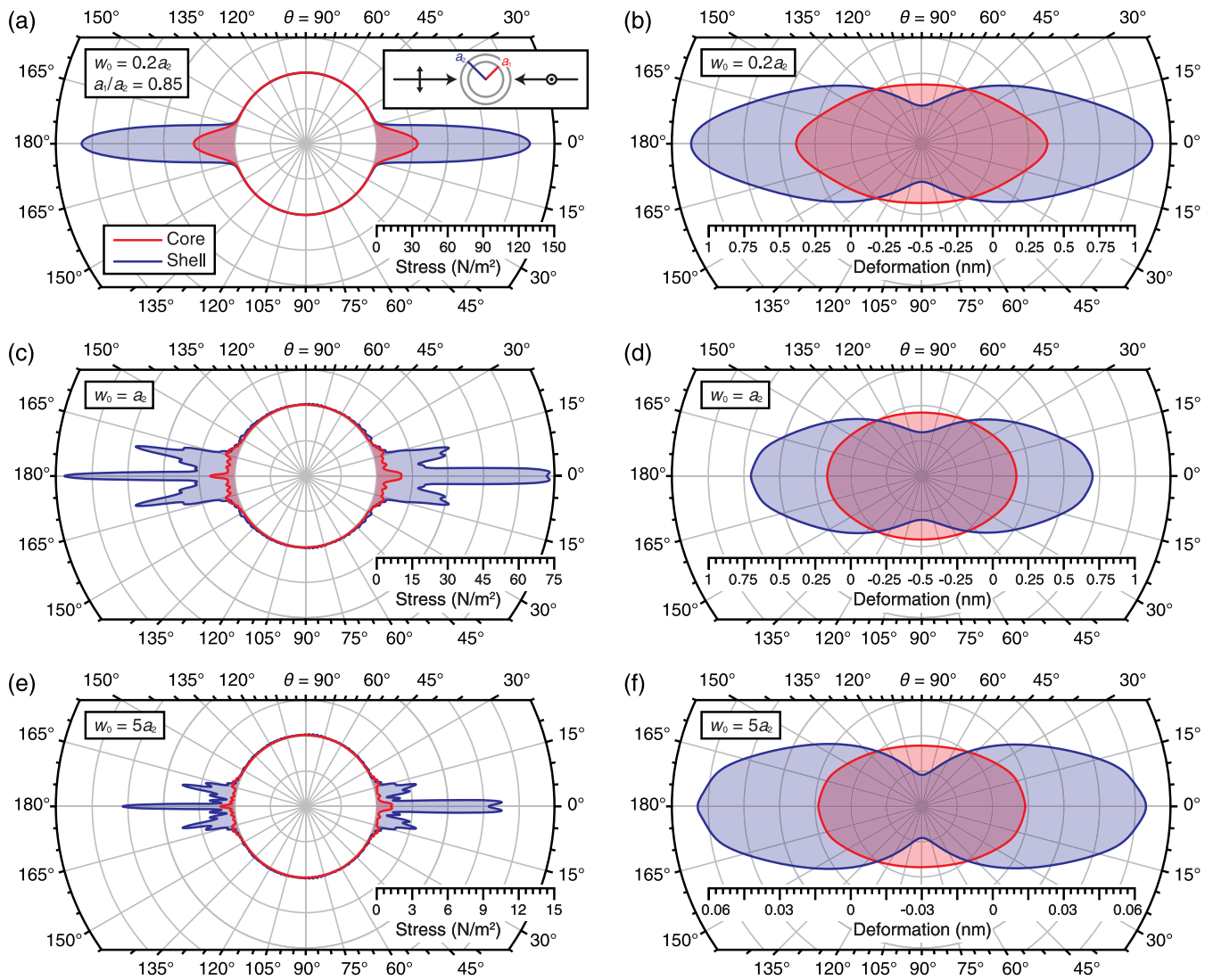


FIG. 4. The stress and deformation on a water-coated organic droplet ($n_1 > n_2$) in the x - z plane induced by two coaxial, counterpropagating Gaussian beams with a shared focal point at the center of the particle. The beams are linearly polarized and mutually orthogonal. The stress and deformation are shown for both the core and the shell. The sphere has a core (shell) refractive index of $n_1 = 1.41$ ($n_2 = 1.33$), an inner (outer) radius of $a_1 = 4.25 \mu\text{m}$ ($a_2 = 5 \mu\text{m}$), and an interfacial (surface) tension of $\gamma_1 = 51 \text{ mN/m}$ ($\gamma_2 = 73 \text{ mN/m}$). The beam waist is increased from $w_0 = 0.2a_2$ in the first row [(a), (b)] to $w_0 = a_2$ in the second row [(c), (d)] and finally to $w_0 = 5a_2$ in the third row [(e), (f)]. In all cases, the power of each Gaussian beam is held constant at $P = 0.1 \text{ W}$ and the beam wavelength is set to $\lambda = 0.532 \mu\text{m}$.

stress consistent with the intensity profile of the Gaussian beam [47].

Another point of comparison within Fig. 2 is the effect of the polarization of the incident beam. Physically, circular polarization makes the stress and deformation azimuthally symmetric, meaning that only $m = 0$ is considered in Eqs. (24) and (27). Whereas for linear polarization, the presence of the $m = 2$ mode breaks this symmetry. It is apparent in Figs. 2(a), 2(c), 2(e), and 2(g) that the different polarization types slightly change the stress profiles when $w_0 = a$ and $w_0 = 5a$ but have little to no impact in the tightly focused beam case. In Figs. 2(b), 2(d), 2(f), and 2(h), the change in polarization has no noticeable effect on the deformation profile for all values of w_0 . This result is not surprising as we have already discussed the smoothing effect of curvature on optical stress and how it affects the deformation.

In Fig. 3, the parameters are such that the incident beam(s) can excite a morphology-dependent resonance (MDR) in the spherical particle. This MDR can be excited by increasing the radius to $a = 5.003 \mu\text{m}$. The ratio of w_0 to a was kept constant and the wavelength and refractive index remained the same as the calculations in Fig. 2. A second-order, transverse electric MDR with a mode number of 66 (the MDR is referred to as TE_{66}^2) is excited by the incident beam(s). MDRs can exhibit strong internal electromagnetic fields near the particle surface [48]. Because Eq. (4) is proportional to the electromagnetic energy density on the interior interface, a substantial amplification of the stress can be seen in the $w_0 = a$ and $w_0 = 5a$ cases, where the MDR is excited, and the supernumerary and “jagged” structures become much more pronounced. For the case of the narrow beam ($w_0 = 0.2a$), no such amplification is observed as the beam does not

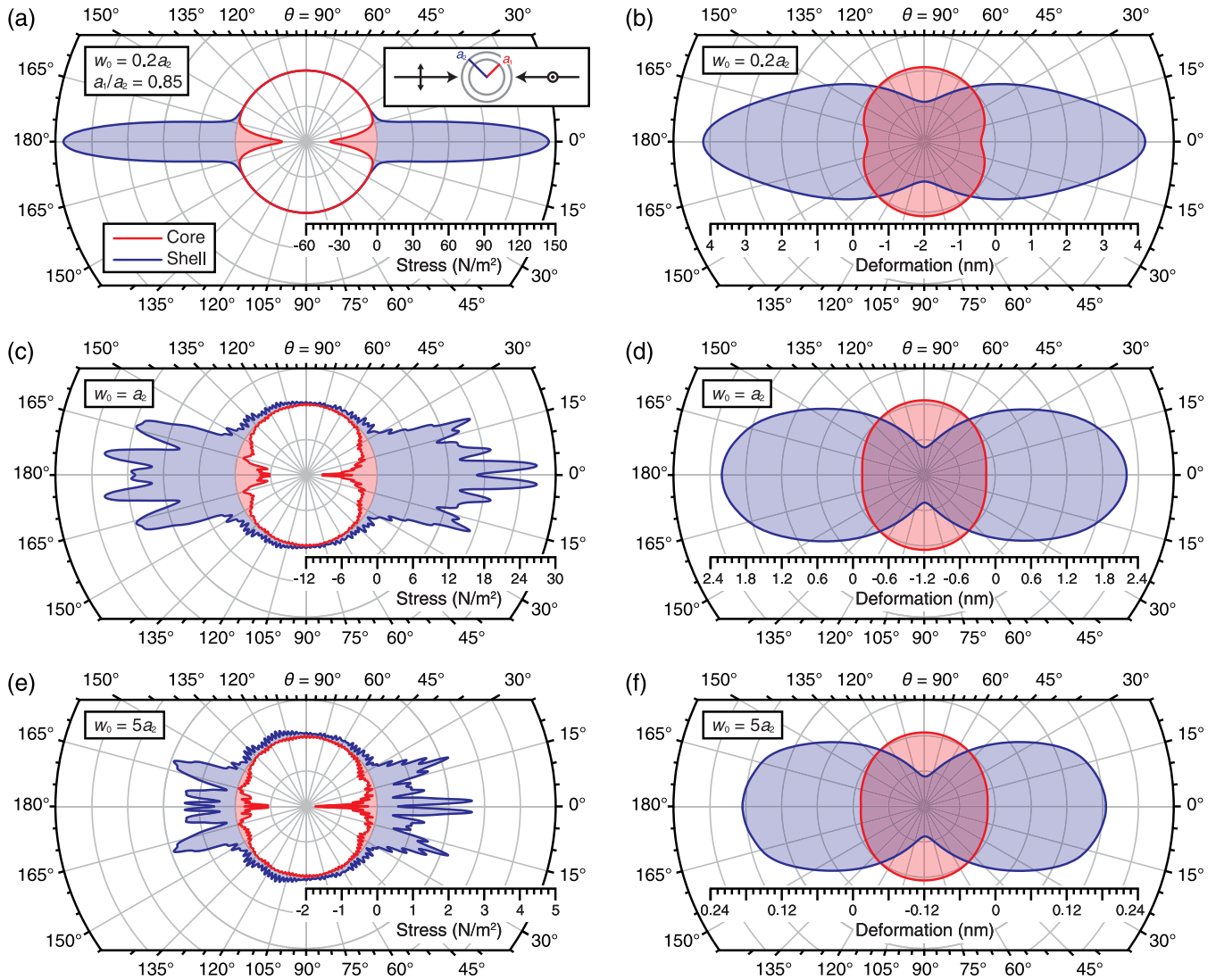


FIG. 5. The stress and deformation on an organic-coated water droplet ($n_2 > n_1$) in the x - z plane. The sphere has a core (shell) refractive index of $n_1 = 1.33$ ($n_2 = 1.41$), an inner (outer) radius of $a_1 = 4.25 \mu\text{m}$ ($a_2 = 5 \mu\text{m}$), and an interfacial (surface) tension of $\gamma_1 = 51 \text{ mN/m}$ ($\gamma_2 = 23 \text{ mN/m}$). The incident beams are described in the caption of Fig. 4.

efficiently excite the MDR. Coupling between the incident beam and the MDR occurs through the evanescent field and is optimal for rays traveling through a point that is located at a radial distance larger than the radius of the sphere [40]. This distance is sometimes referred to as the impact parameter [49]. In the focal plane of the $w_0 = 0.2a$ Gaussian beams examined here, the beam intensity is very small at distances larger than the radius of the sphere so coupling into the MDR is negligible and has no noticeable effect on the optical stress.

B. Core-shell particle in a Gaussian beam

Here, we will examine the stress and resulting deformation of a core-shell particle with an outer radius $a_2 = 5 \mu\text{m}$ and a core-shell ratio $a_1/a_2 = 0.85$ centered on the shared focal point of two coaxial counterpropagating Gaussian beams. We will only consider linearly polarized beams of three different

beam waists. For a core-shell particle, two cases must be considered: (i) The core refractive index is larger than the shell and (ii) the shell refractive index is larger than the core. As a physically relevant core-shell particle, we will use (i) a water-coated organic core and (ii) an organic-coated water core. In the calculations that follow, the organic core or shell will have physical parameters that correspond to decane, as its refractive index, surface tension, and interfacial tension with water are well known. The refractive index of decane is $n = 1.41$ [50]. Depending on whether the water or the organic constitutes the shell, the surface tension of the particle will either correspond to that of (i) $\gamma = 73 \text{ mN/m}$ for the water coating or (ii) $\gamma = 23 \text{ mN/m}$ for the organic coating. In both cases, the interfacial tension between the two components that form the shell and the core is $\gamma = 51 \text{ mN/m}$ [46].

Figure 4 shows the optical stress and deformation of the water shell on an organic core ($n_1 > n_2$). As in the case of the homogeneous sphere, the narrowest beam [Fig. 4(a)] exhibits

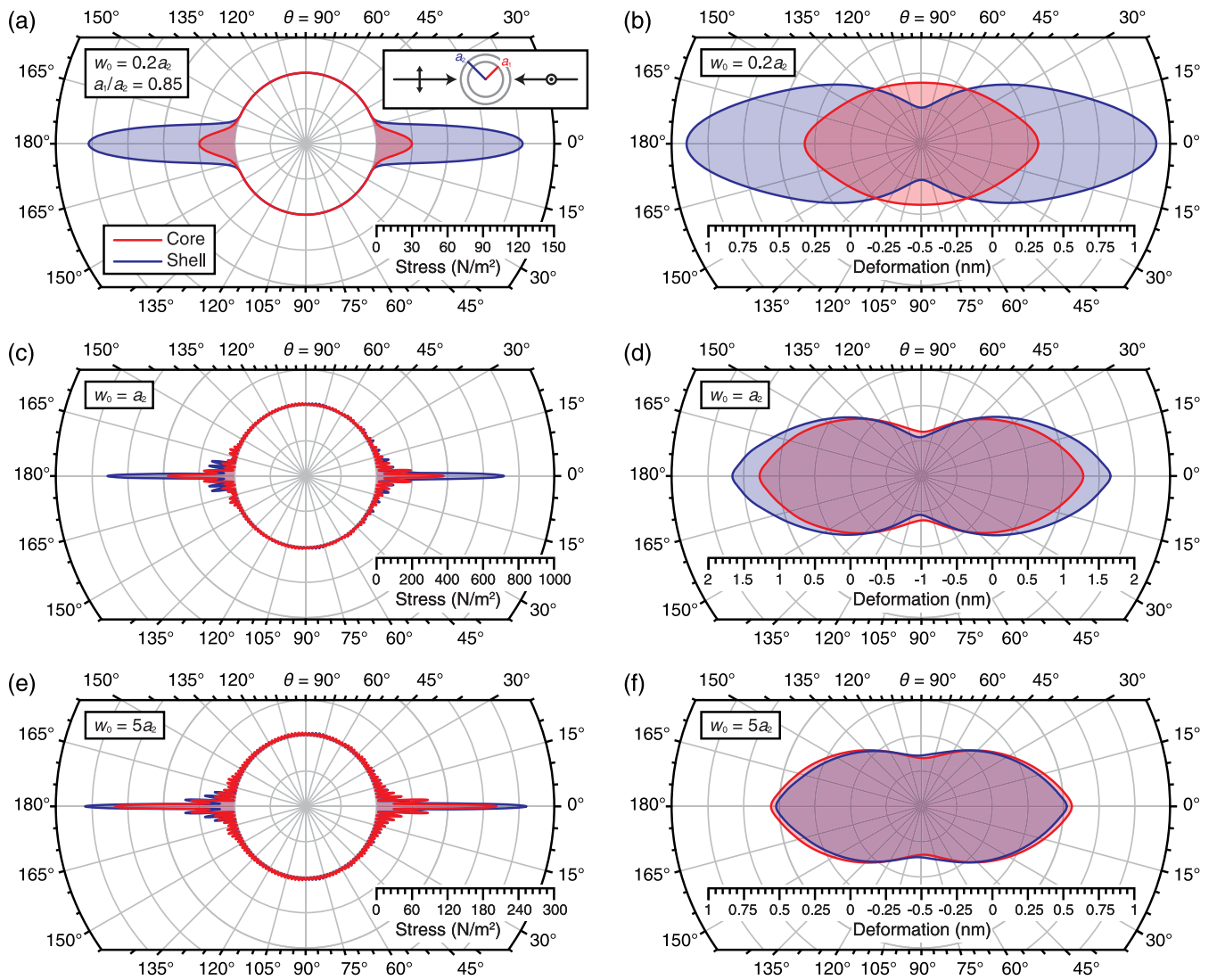


FIG. 6. The stress and deformation on a water-coated organic droplet ($n_1 > n_2$) in the x - z plane. The physical parameters of the droplet are identical to those listed in the caption of Fig. 4. However, the outer radius has been decreased to $a_2 = 4.941 \mu\text{m}$ so that TE_{66}^2 MDR can be excited by the incident beams. The core-shell ratio was unchanged at $a_1/a_2 = 0.85$. The incident beams are described in the caption of Fig. 4.

no interference pattern at the core-shell and shell-medium interface, and the stress profiles on both the core and the shell correlate with the intensity profile of the Gaussian beams. In the absence of any interference effect, the influence of the dielectric contrast from Eqs. (4) and (5) on the optical stress becomes clear. As the dielectric contrast across the core-shell interface is much lower than across the shell-medium surface, the stress on the core is lower than the stress on the shell. In fact, even when interference effects become important, this feature is observed in all of the core-shell calculations (Figs. 4–7). The deformation of the core-shell particle caused by the narrow beams is shown in Fig. 4(b). As expected, the shell deforms more than the core despite the lower interfacial tension with respect to the surface tension. When a beam with a wider beam waist is used, interference patterns in the optical stress appear on both interfaces [Figs. 4(c) and 4(e)]. In the core-shell particle cases considered here, it is interesting to note how the inclusion of the organic core leads to a substantial increase in the stresses in the $\theta = 0^\circ$ and 180°

directions on the shell when compared to the optical stress at the same locations for a homogeneous sphere [Fig. 2(c)]. This is attributed to the core acting as an additional lens that focuses the Gaussian beams.

Figure 5 shows the optical stress and deformation for an organic shell on a water core ($n_2 > n_1$). We observe similar features to the above example in that the stress on the core is consistently smaller than that on the shell [Figs. 5(a), 5(c), and 5(e)]. The most striking feature here is that the higher index of the shell relative to the core results in an inward pointing optical stress at the core-shell interface. Additionally, the core now acts as a diverging lens which is responsible for the broadening of the stress profile on the shell in Figs. 5(c) and 5(e). The resulting deformation in Figs. 5(b), 5(d), and 5(f) consists of the shell being stretched along the axis of the two beams with the core being compressed along the same axis (or stretched along the shared focal plane of the two Gaussian beams). The large shell deformation seen here relative to the examples in Fig. 4 is simply due to the lower surface tension

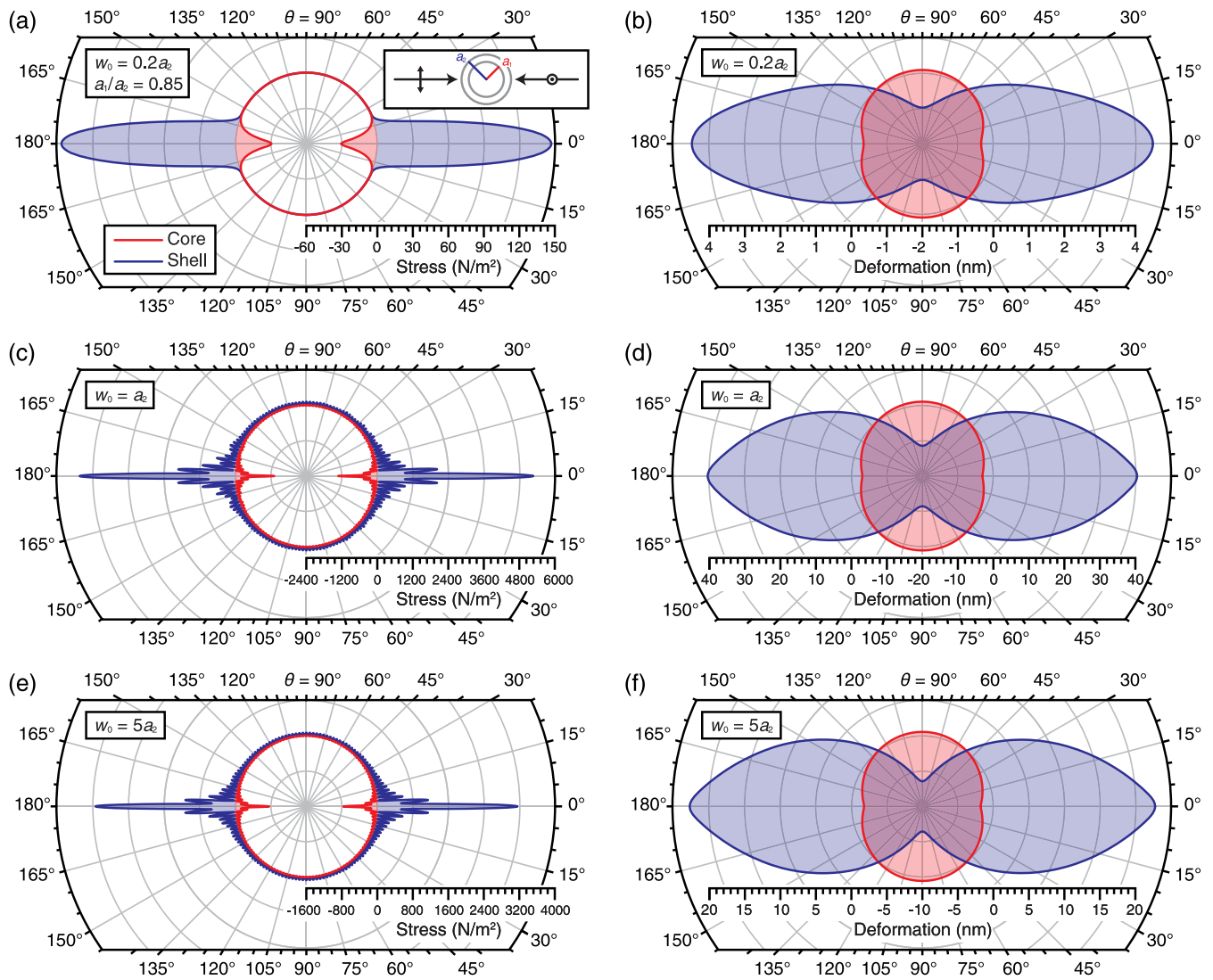


FIG. 7. The stress and deformation on a water-coated organic droplet ($n_2 > n_1$) in the x - z plane. The physical parameters of the droplet are identical to those listed in the caption of Fig. 5. However, the outer radius has been decreased to $a_2 = 4.941 \mu\text{m}$ so that TE_{66}^2 MDR can be excited by the incident beams. The core-shell ratio was unchanged at $a_1/a_2 = 0.85$. The incident beams are described in the caption of Fig. 4.

of the organic shell compared to the previously considered water shell.

Next we examine the effect of exciting the TE_{66}^2 MDR for both $n_1 > n_2$ (Fig. 6) and $n_2 > n_1$ (Fig. 7). The outer radius a_2 that accommodates the MDR for a fixed core-shell ratio $a_1/a_2 = 0.85$ was determined numerically [51]. In the case of the $w_0 = 0.2a_2$ beam waist [shown in Figs. 6(a), 7(a), 6(a), and 6(b)], the MDR is not excited and there is little difference between the off-resonance cases considered in Figs. 4 and 5. The physical reasons for this were discussed earlier when analyzing the optical stress and deformation of a homogeneous sphere. When a MDR is excited, a coated sphere can have strong internal fields in both the core and shell provided the shell is not too thick with respect to the core. As anticipated for beam waists that can excite the TE_{66}^2 MDR, there is an increase in the stress on both the core and the shell and the subsequent deformation is enhanced [Figs. 6(c)–6(f) and Figs. 7(c)–7(f)].

C. Homogeneous spherical particle in a Bessel beam

The optical Bessel beam can be represented as a superposition of plane waves forming a cone of semiapex angle θ_0 [15,52]. Using this description, analytic expressions for the GLMT BSCs of a zeroth-order Bessel beam can be determined (see Appendix B). Figure 8 shows the stress and deformation of a homogeneous droplet centered on the beam axis of either a single Bessel beam or two coaxial counter-propagating Bessel beams at three different semiapex angles. For the single Bessel beam, increasing the semiapex angle leads to increased optical stress in the $\theta = 180^\circ$ direction [Fig. 8(a)]. Note that for all of the examples in Fig. 8, the net optical force will be positive. So, while the particle is deformed in the direction opposite to the direction of Bessel beam propagation in Fig. 8(b), it would still be pushed along the direction of the propagating beam (no predicted optical pulling). In Figs. 8(c) and 8(d), the effect of having two coaxial and counterpropagating beams leads to the expected

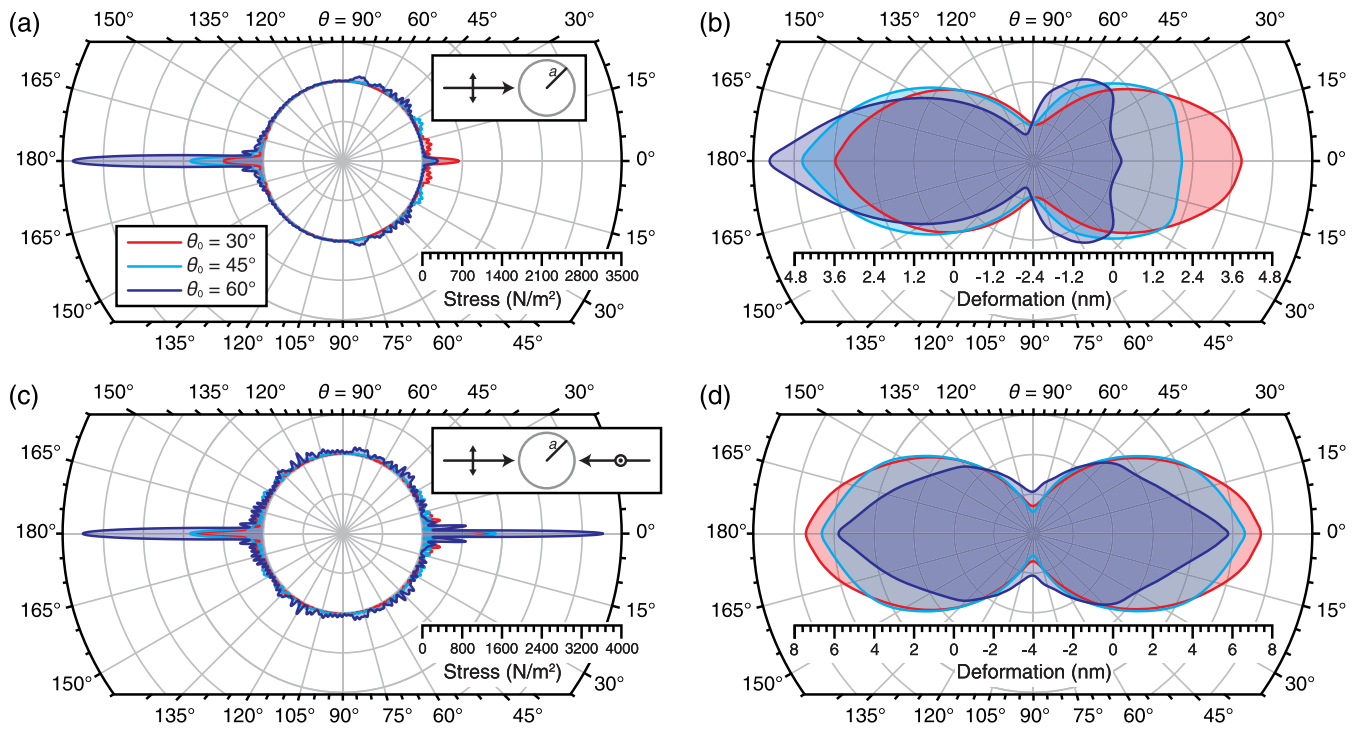


FIG. 8. The stress and deformation in the x - z plane induced by one or two zeroth-order Bessel beams on a homogeneous sphere with physical parameters that are identical to those listed in the caption of Fig. 2. The first row [(a), (b)] shows the case of an x -polarized beam coming from $\theta = 180^\circ$. The second row [(c), (d)] shows the case of one x -polarized Bessel beam coming from $\theta = 180^\circ$ and one y -polarized Bessel beam coming from $\theta = 0^\circ$. In all cases, each Bessel beam has a fixed power of $P = 0.1$ W and a wavelength of $\lambda = 0.532$ μm .

result of optical stretching along the shared axis of the beams.

Figure 9 shows the net force in the z direction on a homogeneous sphere centered on the axis of a single Bessel beam as the radius of the sphere changes. Here, we have included a plot for a very high semiapex angle ($\theta_0 = 80^\circ$). It can be seen that optical pulling can be achieved for several narrow ranges of radii. This is not possible for the smaller semiapex angles (e.g., $\theta_0 = 60^\circ$ is shown in Fig. 9). However,

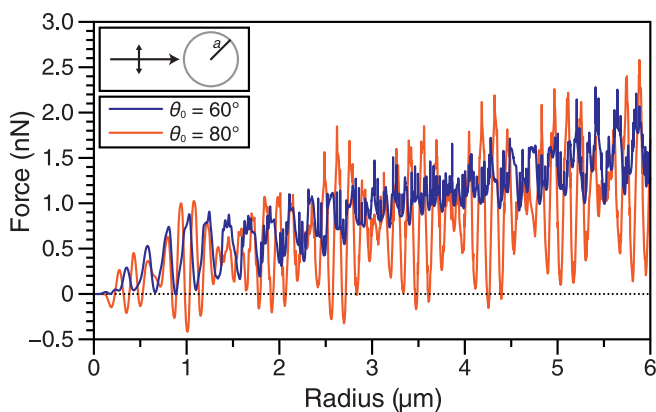


FIG. 9. The net force in the z direction imparted by an x -polarized zeroth-order Bessel beam on a homogeneous sphere with a refractive index of $n = 1.33$ across a range of radii, a . The semiapex angle of the Bessel beam is either $\theta_0 = 60^\circ$ or 80° . In both cases, the Bessel beam has a fixed power of $P = 0.1$ W and a wavelength of $\lambda = 0.532$ μm .

even for $\theta_0 = 80^\circ$, as the radius becomes much larger than the wavelength of the incident light, the net force is always in the positive z direction and optical pulling can no longer be realized. In Fig. 9, a longer period envelope also appears over the more rapid oscillations in force as a function of radius. This is most distinct in the $\theta_0 = 80^\circ$ curve. Calculations reveal that this is the well-known Mie interference structure [53].

Figures 10(a) and 10(b) compare the stress and deformation for three spheres with similar radii that experience very different net optical forces. The radii are all in a region of the $\theta_0 = 80^\circ$ curve in Fig. 9 where the net force rapidly changes between optical pushing and pulling. Therefore, small changes to the radii allow us to examine the stress and deformation during (i) optical pulling, (ii) optical pushing, and (iii) the case where the net optical force is zero. At such a large semiapex angle, the optical stress on the lateral sides of the sphere lead to a significant deformation in the direction perpendicular to the beam axis. This is perhaps surprising as there are large optical stresses in the $\theta = 0^\circ$ and 180° directions, but it can be attributed to the fact that most of the beam momentum is along the x axis. It then follows that the particle must stretch more along the x axis instead of the z axis. Whether or not the net force is zero or leads to pushing or pulling does not qualitatively change any of the results in Figs. 10(a) and 10(b). In Figs. 10(c) and 10(d), the same set of radii are studied for the case where a second, counterpropagating Bessel beam has been added. The main result here is that, unlike earlier examples in this work [e.g., Figs. 2(c) and 2(d)], the counterpropagating beams can now be thought of as compressing the particle rather than stretching it.

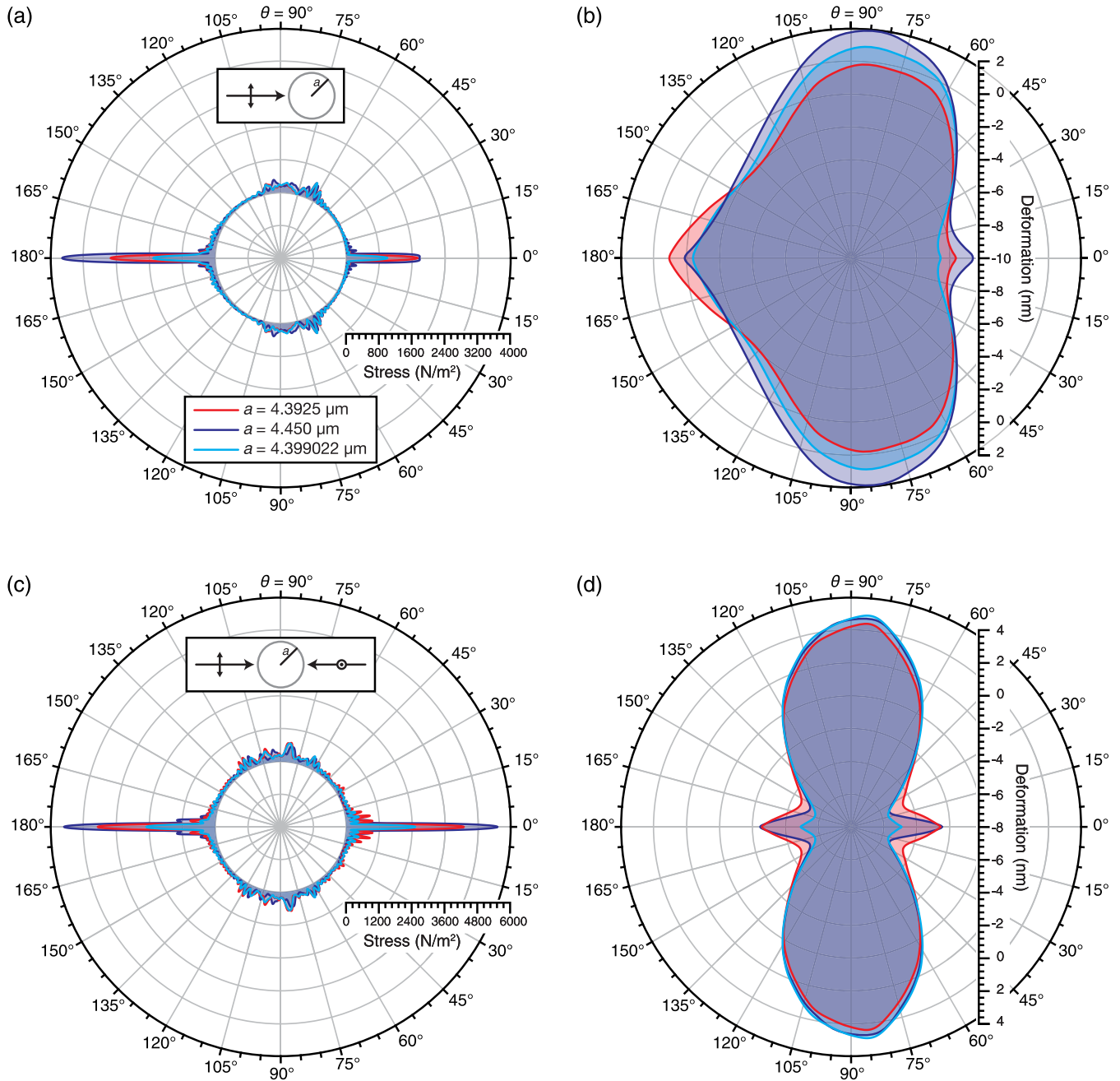


FIG. 10. The stress and deformation in the x - z plane induced by one or two linearly polarized zeroth-order Bessel beams on a homogeneous sphere with physical parameters that are identical to those listed in the caption of Fig. 2 except with differing radii [indicated in the inset of panel (a)]. The first row [(a), (b)] shows the case of an x polarized beam coming from $\theta = 180^\circ$. The second row [(c), (d)] shows the case of one x polarized beam coming from $\theta = 180^\circ$ and one y polarized beam coming from $\theta = 0^\circ$. Here, for the single beam, three cases are shown: negative net force (pulling), zero net force, and positive net force (pushing). In all cases, each Bessel beam has a fixed power of $P = 0.1$ W and a wavelength of $\lambda = 0.532 \mu\text{m}$.

D. Core-shell particle in a Bessel beam

Figure 11 examines the net force on both the core and shell of a core-shell particle as a function of shell radius for a large semiapex angle ($\theta_0 = 80^\circ$). The total force on the core-shell particle is also calculated. When $n_1 < n_2$, it can be seen that the core is pulled by the beam whereas the shell is pushed due to the lower refractive index of the core [Fig. 11(a)]. A peculiar feature is that whenever the net optical force dips

below zero, the core is pushed while the shell is pulled. For the case when $n_1 > n_2$, whenever the net force is below zero, both the core and shell are pulled toward the beam [Fig. 11(b)]. As in the homogeneous case, the ranges of radii where optical pulling is possible are limited and become nonexistent at large radius. Finally, in Fig. 12, we examine one case of optical stress and deformation for the core-shell particle in a Bessel beam. The chosen radius corresponds to one of the regions on Fig. 11(a), where each Bessel beam pulls the core-shell

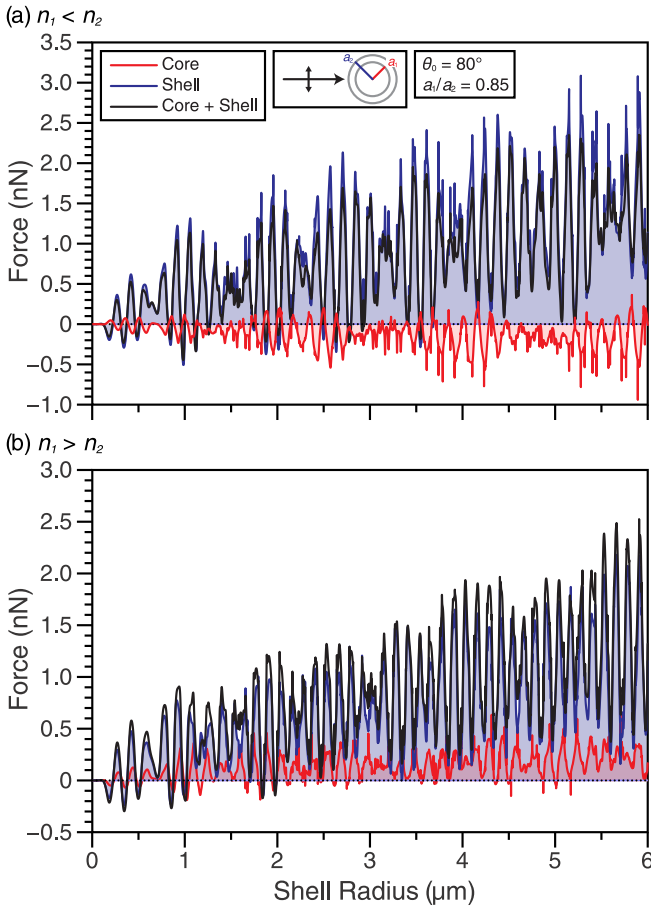


FIG. 11. The net force in the z direction imparted by an x -polarized zeroth-order Bessel beam on a core-shell particle across a range of outer radii a_2 . In all calculations, $a_1/a_2 = 0.85$. The semiapex angle of the Bessel beam is $\theta_0 = 80^\circ$, its beam power is $P = 0.1$ W, and its wavelength is $\lambda = 0.532 \mu\text{m}$. Both the net force on the core and the net force on the shell are shown. The total force is also shown and is the sum of the force on the core and shell. The first row (a) shows the case when $n_1 = 1.33$ and $n_2 = 1.41$. The second row (b) shows the opposite case, $n_1 = 1.41$ and $n_2 = 1.33$.

particle. Along the axis of propagation, the broader stress profile on the shell leads to a stretching deformation unlike its homogeneous counterpart [Fig. 10(d)]. In addition, the optical stress will also deform the shell along the perpendicular axis. The resulting deformation combines these two effects and, due to the assumption of conservation of volume, this will lead to a compression of the shell along the axes where the stress is the lowest.

V. CONCLUSION

We have presented a theoretical model for the optical stress and deformation induced by an arbitrary incident beam for a particle composed of concentric spherical shells. The electromagnetic component of the problem is treated in the framework of GLMT where the electromagnetic field is expanded in a basis of VSWFs. Then, by applying the stress-balance equation on the static surface (and core-shell interface) of the particle, an analytic expression for the optical

deformation is derived. Using this theoretical framework, we investigate the deformation of homogeneous and core-shell spherical droplets by on-axis Gaussian beam(s) and zeroth-order Bessel beam(s).

To our knowledge, the optical stress and deformation of core-shell particles had never been previously studied. Interesting results for the core-shell sphere include the role that the relative refractive index of the core and shell play in terms of optical stress and deformation. If $n_1 < n_2$, two counterpropagating Gaussian beam will compress the core and stretch the shell. If $n_2 < n_1$, both the core and the shell will be stretched. When the Gaussian beams are replaced by Bessel beams with high semiapex angle, it was found that for $n_1 < n_2$ the shell stretches along both the axes parallel and perpendicular to the beam. Compression then occurs where the stress distribution is the lowest. Results related to the excitation of MDRs were consistent with expectations based on previous studies (i.e., increased optical stress if an MDR is excited and MDRs are not excited by narrow beam waists).

For the zeroth-order Bessel beam calculations, when a homogeneous sphere is centered on the beam axis of two coaxial counterpropagating beams with high semiapex angles ($\theta_0 = 80^\circ$), the beams will compress rather than stretch the particle along the shared beam axis. Reducing the semiapex angle of the Bessel beams ($\theta_0 = 30^\circ, 45^\circ$, and 60°) gives the same qualitative result as the Gaussian beam case (the particle is stretched by the beams). Similar results were found for the core-shell system in the Bessel beam.

We would like to emphasize that with the analytic solution presented here, calculations are not computationally demanding and the optical stress and deformation model can readily be applied to systems with very large size parameters or to particles composed of additional concentric spherical shells. This is because the analytic solution is written in terms of the Wigner $3j$ symbols, and as we have already discussed, recursion relations allow for the accurate and efficient calculation of the Wigner $3j$ symbols. These can be subsequently stored and used in the aforementioned systems.

One final question that needs to be addressed is whether the nonsphericity of the deformed particles leads to a significant change in their internal field distribution and subsequent optical deformation. We used the T -matrix method to investigate this question by computing the optical stress profile on the deformed surfaces [54]. It was found that, in nonresonant cases, the minor change in the stress profile that was caused by the small surface deformation did not significantly alter the results presented here using the spherical assumption. But, for cases where a sharp MDR was excited by the incident beam, this was no longer true. This is because the resonant position of the MDR will shift as the particle deforms and the stress will decrease when the MDR is no longer excited by the incident beam. However, T -matrix calculations also revealed that, if the wavelength of the incident beam was adjusted to match the shifted MDR in the deformed particle, excellent agreement between the spherical calculation and the T -matrix calculation would be achieved. Therefore, the calculations in this work are accurate even when the deformations are accounted for, but it should be recognized that listed MDR positions are for spherical particles and will need to be slightly modified so that MDR excitations still occur in deformed particles.

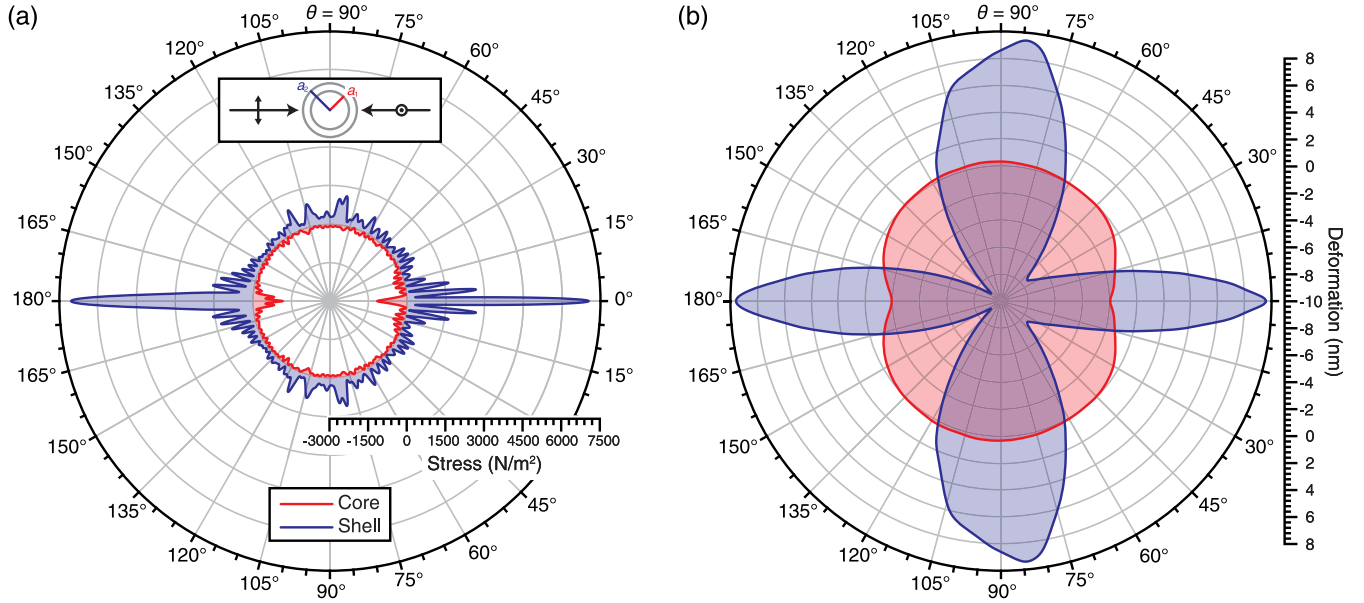


FIG. 12. The stress and deformation in the x - z plane induced by two coaxial, counterpropagating zeroth-order Bessel beams on a core-shell particle with physical parameters that are identical to those listed in the caption of Fig. 5 except that the outer radius was changed to $a_2 = 3.5447\mu\text{m}$ so that each beam pulls the particle. The beams are linearly polarized and their polarizations are orthogonal. The stress is shown on the left (a) and the resulting deformation on the right (b). These are shown for both the core and the shell. The Bessel beam has a fixed power of $P = 0.1$ W and a wavelength of $\lambda = 0.532\mu\text{m}$.

ACKNOWLEDGMENT

T.C.P. acknowledges support from the Natural Sciences and Engineering Research Council of Canada (NSERC).

APPENDIX A: BEAM-SHAPE COEFFICIENTS OF A GAUSSIAN BEAM

The BSCs of a Gaussian beam are calculated using the localization principle [40]. The beam center is located at (x_f, y_f, z_f) with respect to the center of origin of the particle and the beam waist is w_0 . The BSCs are then

$$g_{lm}^{\text{TM}} = \begin{cases} \frac{F_l}{2} \left(\frac{-r_f^+}{l+\frac{1}{2}} \right)^{|m|-1} [J_{|m|-1}(Q_l) - (r_f^+)^2 J_{|m|+1}(Q_l)] & \text{if } (m < 0), \\ F_l \frac{l(l+1)}{l+\frac{1}{2}} \frac{x_f}{(x_f^2+y_f^2)^{1/2}} J_1(Q_l) & \text{if } (m = 0), \\ \frac{F_l}{2} \left(\frac{-r_f^-}{l+\frac{1}{2}} \right)^{|m|-1} [J_{|m|-1}(Q_l) - (r_f^-)^2 J_{|m|+1}(Q_l)] & \text{if } (m > 0). \end{cases} \quad (\text{A1})$$

$$g_{lm}^{\text{TE}} = \begin{cases} \frac{F_l}{2i} \left(\frac{-r_f^+}{l+\frac{1}{2}} \right)^{|m|-1} [J_{|m|-1}(Q_l) + (r_f^+)^2 J_{|m|+1}(Q_l)] & \text{if } (m < 0), \\ F_l \frac{l(l+1)}{l+\frac{1}{2}} \frac{y_f}{(x_f^2+y_f^2)^{1/2}} J_1(Q_l) & \text{if } (m = 0), \\ \frac{F_l}{2i} \left(\frac{-r_f^-}{l+\frac{1}{2}} \right)^{|m|-1} [J_{|m|-1}(Q_l) + (r_f^-)^2 J_{|m|+1}(Q_l)] & \text{if } (m > 0). \end{cases} \quad (\text{A2})$$

The terms that appear in Eqs. (A1) and (A2) are

$$F_l = D \exp \left[-D \left(\frac{x_f^2 + y_f^2}{w_0^2} \right) - Ds^2 \left(l + \frac{1}{2} \right)^2 - \frac{i}{s} \frac{z_f}{w_0} \right],$$

$$Q_l = - \left(l + \frac{1}{2} \right) \left(\frac{x_f^2 + y_f^2}{z_f^2} \right)^{1/2} \left(1 + \frac{iw_0}{2sz_f} \right)^{-1},$$

$$r_f^\pm = \frac{x_f \pm iy_f}{(x_f^2 + y_f^2)^{1/2}}, \quad D = \left(1 - \frac{2isz_f}{w_0} \right)^{-1}, \quad s = \frac{1}{kw_0},$$

and $J_m(Q_l)$ is the cylindrical Bessel function of the first kind. m is an integer that denotes the order of the Bessel function.

APPENDIX B: BEAM-SHAPE COEFFICIENTS OF A ZERO-ORDER BESSEL BEAM

The fields for a zeroth-order Bessel beam are given by [52,55]

$$\mathbf{E}(\mathbf{r}) = E_{B0} e^{ik_z z} \{ [J_0(\sigma) + P_{\perp} J_2(\sigma) \cos(2\phi)] \hat{\mathbf{e}}_x + P_{\perp} J_2(\sigma) \sin(2\phi) \hat{\mathbf{e}}_y - i2P_{\parallel} J_1(\sigma) \cos \phi \hat{\mathbf{e}}_z \}, \quad (\text{B1})$$

$$Z_0 \mathbf{H}(\mathbf{r}) = E_{B0} e^{ik_z z} \{ P_{\perp} J_2(\sigma) \sin(2\phi) \hat{\mathbf{e}}_x + [J_0(\sigma) - P_{\perp} J_2(\sigma) \cos(2\phi)] \hat{\mathbf{e}}_y - i2P_{\parallel} J_1(\sigma) \sin \phi \hat{\mathbf{e}}_z \}, \quad (\text{B2})$$

where $\sigma = k\rho \sin \theta_0$, $\phi = \arctan(x/y)$, $\rho = \sqrt{x^2 + y^2}$, $P_{\perp} = (1 - \cos \theta_0)/(1 + \cos \theta_0)$, $P_{\parallel} = (\sin \theta_0)/(1 + \cos \theta_0)$, and θ_0 is the semiapex angle.

The time-averaged Poynting vector is

$$\langle \mathbf{S} \rangle = \frac{1}{2} \text{Re}[\mathbf{E} \times \mathbf{H}^*] = \frac{E_{B0}^2}{2Z_0} [J_0^2(\sigma) - P_{\perp}^2 J_2^2(\sigma)] \hat{\mathbf{e}}_z. \quad (\text{B3})$$

The x and y components of the time-averaged Poynting vector are vanishing because the terms that arise are imaginary. In effect, the energy flux of the Bessel beam is in the z direction. The central core of the Bessel beam is defined by setting the z component of the time-averaged Poynting vector to zero. In this way, the Bessel beam core is defined as

$$r_{\text{bes}} = \frac{\sigma_0}{k \sin \theta_0} = \frac{\sigma_0}{k_r}, \quad (\text{B4})$$

where σ_0 is the first root of the transcendental equation

$$J_0^2(\sigma_0) - P_{\perp}^2 J_2^2(\sigma_0) = 0. \quad (\text{B5})$$

The total power of the core can be found by integrating the time-averaged Poynting vector over the area of the core

$$P_{\text{bes}} = 2\pi \int_0^{r_{\text{bes}}} S_z(k_r \rho) \rho d\rho = \frac{\pi E_{B0}^2}{Z_0} \int_0^{r_{\text{bes}}} [J_0^2(k_r \rho) - P_{\perp}^2 J_2^2(k_r \rho)] \rho d\rho. \quad (\text{B6})$$

Using Lommel's integral,

$$\int_0^{r_{\text{bes}}} J_v^2(k_r \rho) \rho d\rho = \frac{r_{\text{bes}}^2}{2} [J_v^2(k_r r_{\text{bes}}) - J_{v-1}(k_r r_{\text{bes}}) J_{v+1}(k_r r_{\text{bes}})], \quad (\text{B7})$$

as well as Eq. (B5) and the fact that $J_{-1} = -J_1$, we find

$$P_{\text{bes}} = \frac{\pi E_{B0}^2}{2 Z_0} r_{\text{bes}}^2 \left[\left(1 - \frac{P_{\perp}^2}{4}\right) J_1^2(\sigma_0) + \frac{P_{\perp}^2}{2} J_1(\sigma_0) J_3(\sigma_0) - \frac{P_{\perp}^2}{4} J_3^2(\sigma_0) \right], \quad (\text{B8})$$

In order to compute the optical stress and deformation on a sphere located at $\mathbf{r}_0 = (x_0, y_0, z_0)$ by an incident Bessel beam, its BSCs need to be determined by expanding the field in SVWFs [Eq. (6)]. Instead of using Eqs. (B1) and (B2) to calculate the electromagnetic field, the Bessel beam is reformulated as a sum of plane waves forming a cone of semiapex angle θ_0 and propagating along the z axis [41]. Assuming the Bessel beam is x polarized, the field is given by

$$\mathbf{E}(\mathbf{r}) = E_0 \int_0^{2\pi} \mathbf{e}_0(\theta, \phi) e^{i\mathbf{k} \cdot \mathbf{r}} d\phi, \quad (\text{B9})$$

where $\mathbf{e}_0 = \cos \phi \hat{\mathbf{e}}_x - \sin \phi \hat{\mathbf{e}}_y$ and $E_0 = E_{B0}/[\pi(1 + \cos \theta_0)]$. The BSCs of the plane waves expanded about the sphere located at \mathbf{r}_0 are [56]

$$p_{mn} = U_n [\cos \phi \tilde{\tau}_{mn}(\cos \theta_0) - im \sin \phi \tilde{\pi}_{mn}(\cos \theta_0)] e^{im\phi} e^{i\mathbf{k} \cdot \mathbf{r}_0}, \quad (\text{B10})$$

$$q_{mn} = U_n [m \cos \phi \tilde{\pi}_{mn}(\cos \theta_0) - i \sin \phi \tilde{\tau}_{mn}(\cos \theta_0)] e^{im\phi} e^{i\mathbf{k} \cdot \mathbf{r}_0}, \quad (\text{B11})$$

$$U_n = \frac{4\pi i^n}{n(n+1)}, \quad (\text{B12})$$

and $\tilde{\pi}_{mn}$, $\tilde{\tau}_{mn}$ are normalized π_{mn} and τ_{mn} functions. Since the notation used differs from ours, we find the following conversion:

$$g_{lm}^{\text{TM}}(\phi) = \frac{(l - |m|)!}{(l + |m|)!} [\cos \phi \tau_l^{|m|}(\cos \theta_0) + im \sin \phi \pi_l^{|m|}(\cos \theta_0)] e^{im\phi} e^{i\mathbf{k} \cdot \mathbf{r}_0}, \quad (\text{B13})$$

$$g_{lm}^{\text{TE}}(\phi) = \frac{(l - |m|)!}{(l + |m|)!} [\sin \phi \tau_l^{|m|}(\cos \theta_0) - im \cos \phi \pi_l^{|m|}(\cos \theta_0)] e^{im\phi} e^{i\mathbf{k} \cdot \mathbf{r}_0}. \quad (\text{B14})$$

where we indicate a ϕ dependence to emphasize that these BSCs go into the integral

$$g_{lm}^{\text{TM}} = \frac{(l - |m|)!}{(l + |m|)!} \int_0^{2\pi} d\phi [\cos \phi \tau_l^{|m|}(\cos \theta_0) + im \sin \phi \pi_l^{|m|}(\cos \theta_0)] e^{im\phi} e^{i\mathbf{k}\cdot\mathbf{r}_0}, \quad (\text{B15})$$

$$g_{lm}^{\text{TE}} = \frac{(l - |m|)!}{(l + |m|)!} \int_0^{2\pi} d\phi [\sin \phi \tau_l^{|m|}(\cos \theta_0) - im \cos \phi \pi_l^{|m|}(\cos \theta_0)] e^{im\phi} e^{i\mathbf{k}\cdot\mathbf{r}_0}. \quad (\text{B16})$$

Expanding $e^{i\mathbf{k}\cdot\mathbf{r}_0}$ using $\rho_0 = k\sqrt{x_0^2 + y_0^2} \sin \theta_0$ and $\phi_0 = \arctan(-y_0/x_0) - (\pi/2)$, the integrals are solved analytically [41]. The final result is

$$g_{lm}^{\text{TM}} = \frac{(l - |m|)!}{(l + |m|)!} e^{ikz_0 \cos \theta_0} [\tau_l^{|m|}(\cos \theta_0) I^+ + im \pi_l^{|m|}(\cos \theta_0) I^-], \quad (\text{B17})$$

$$g_{lm}^{\text{TE}} = \frac{(l - |m|)!}{(l + |m|)!} e^{ikz_0 \cos \theta_0} [\tau_l^{|m|}(\cos \theta_0) I^- - im \pi_l^{|m|}(\cos \theta_0) I^+], \quad (\text{B18})$$

with I^\pm given by

$$I^\pm = \pi [e^{i(m-1)\phi_0} J_{1-m}(\rho_0) \pm e^{i(m+1)\phi_0} J_{-1-m}(\rho_0)]. \quad (\text{B19})$$

A final note is that in calculating the stress induced by a Bessel beam, the plane-wave representation is used. Accordingly, the field amplitude of the beam E_0 is calculated using Eq. (B8) and $E_0 = E_{B0}/[\pi(1 + \cos \theta_0)]$ to yield

$$E_0 = \frac{1}{\pi(1 + \cos \theta_0)} \left(\frac{2Z_0 P_{\text{bes}}}{\pi r_{\text{bes}}^2} \right)^{1/2} \left[\left(1 - \frac{P_\perp^2}{4} \right) J_1^2(\sigma_0) + \frac{P_\perp^2}{2} J_1(\sigma_0) J_3(\sigma_0) - \frac{P_\perp^2}{4} J_3^2(\sigma_0) \right]^{-1/2}. \quad (\text{B20})$$

APPENDIX C: THE OVERLAP INTEGRAL OF THREE ANGULAR FUNCTIONS

1. Solution of the first integral

As stated, the azimuthal mode numbers are related by $m = m_1 - m_2$. However, Eqs. (40)–(42) involve the absolute value of the azimuthal mode numbers. This is a consequence of the convention used in defining the SVWFs in Eqs. (7) and (8). It can be corrected by using the fact that

$$P_l^{|m|} = \begin{cases} (-1)^m \frac{(l+|m|)!}{(l-|m|)!} P_l^m & \text{if } (m < 0), \\ P_l^m & \text{if } (m \geq 0), \end{cases} \quad (\text{C1})$$

and let p_{lm} be

$$p_{lm} = \begin{cases} (-1)^m \frac{(l+|m|)!}{(l-|m|)!} & \text{if } (m < 0), \\ 1 & \text{if } (m \geq 0), \end{cases} \quad (\text{C2})$$

such that

$$\mathcal{I}_{l_1 l_2 m_1 m_2 l m}^A = p_{l_1 m_1} p_{l_2 m_2} p_{lm} \int_0^\pi \sin \theta d\theta P_{l_1}^{m_1} P_{l_2}^{m_2} P_l^m. \quad (\text{C3})$$

Since $m_1 = m_2 + m$, the product of the two rightmost associated Legendre polynomials is given by [57]

$$P_{l_1}^{m_2} P_l^m = (-1)^{m_1} \sqrt{\frac{(l_2 + m_2)! (l + m)!}{(l_2 - m_2)! (l - m)!}} \sum_{l_i} G_i \sqrt{\frac{(l_i - m_1)!}{(l_i + m_1)!}} P_{l_i}^{m_1}, \quad (\text{C4})$$

where

$$G_i = (-1)^{m_1} (2l_i + 1) \begin{pmatrix} l_2 & l & l_i \\ 0 & 0 & 0 \end{pmatrix} \begin{pmatrix} l_2 & l & l_i \\ m_2 & m & -m_1 \end{pmatrix}, \quad (\text{C5})$$

and is nonzero provided that (1) $|l_2 - l| \leq l_i \leq l_2 + l$, (2) $l_i \geq |m_1|$, and (3) $l_i + l_2 + l$ are even. The quantities in parentheses are Wigner $3j$ symbols. If we insert the expansion given in Eq. (C4) into the integral Eq. (C3) and use the orthogonality of the

associated Legendre polynomials

$$\int_0^\pi \sin \theta d\theta P_{l_1}^{m_1} P_{l_2}^{m_2} = \frac{2}{2l_1 + 1} \frac{(l_1 + m_1)!}{(l_1 - m_1)!} \delta_{l_1, l_2}, \quad (\text{C6})$$

then the integral can be expressed as

$$\mathcal{I}_{l_1 l_2 m_1 l_2 m_2}^A = p_{l_1 m_1} p_{l_2 m_2} p_{lm} \left(2(-1)^{m_1} \sqrt{\frac{(l_1 + m_1)!(l_2 + m_2)!(l + m)!}{(l_1 - m_1)!(l_2 - m_2)!(l - m)!}} \begin{pmatrix} l_2 & l & l_1 \\ 0 & 0 & 0 \end{pmatrix} \begin{pmatrix} l_2 & l & l_1 \\ m_2 & m & -m_1 \end{pmatrix} \right). \quad (\text{C7})$$

The Wigner $3j$ symbols obey the following permutation relations

$$\begin{pmatrix} j_1 & j_2 & j_3 \\ m_1 & m_2 & m_3 \end{pmatrix} = \begin{pmatrix} j_3 & j_1 & j_2 \\ m_3 & m_1 & m_2 \end{pmatrix}, \quad (\text{C8})$$

$$\begin{pmatrix} j_1 & j_2 & j_3 \\ m_1 & m_2 & m_3 \end{pmatrix} = (-1)^{j_1 + j_2 + j_3} \begin{pmatrix} j_1 & j_2 & j_3 \\ -m_1 & -m_2 & -m_3 \end{pmatrix}. \quad (\text{C9})$$

Using these relations and expanding the coefficients p_{lm} gives

$$\mathcal{I}_{l_1 l_2 m_1 l_2 m_2}^A = 2(-1)^\Lambda \sqrt{\frac{(l_1 + |m_1|)!(l_2 + |m_2|)!(l + |m|)!}{(l_1 - |m_1|)!(l_2 - |m_2|)!(l - |m|)!}} \begin{pmatrix} l_1 & l_2 & l \\ 0 & 0 & 0 \end{pmatrix} \begin{pmatrix} l_1 & l_2 & l \\ m_1 & -m_2 & -m \end{pmatrix}, \quad (\text{C10})$$

where $\Lambda = m_1 + \sum_{m_i < 0} m_i$. Note that due to the properties of the Wigner $3j$ symbols, Eq. (C10) is nonzero when $l_1 + l_2 + l$ is even and when the triangle equality $|l_1 - l_2| \leq l \leq l_1 + l_2$ is satisfied.

Wigner $3j$ symbols are related to the Clebsch-Gordan coefficients

$$\langle l_1 m_1 l_2 m_2 | l m \rangle = (-1)^{l_1 + l_2 - m} \sqrt{2l + 1} \begin{pmatrix} l_1 & l_2 & l \\ m_1 & m_2 & -m \end{pmatrix}, \quad (\text{C11})$$

which in turn are given by Racah's formula [58]

$$\langle l_1 m_1 l_2 m_2 | l m \rangle = \delta_{m, m_1 + m_2} \sqrt{(2l + 1)AB} \sum_\nu \frac{(-1)^\nu}{\nu! C_\nu}, \quad (\text{C12})$$

where

$$A = \frac{(l_1 + l_2 - l)!(l_2 + l - l_1)!(l + l_1 - l_2)!}{(l_1 + l_2 + l + 1)!},$$

$$B = (l_1 + m_1)!(l_1 - m_1)!(l_2 + m_2)!(l_2 - m_2)!(l + m)!(l - m)!,$$

$$C_\nu = (l_1 + l_2 - l - \nu)!(l_1 - m_1 - \nu)!(l_2 + m_2 - \nu)!(l - l_2 + m_1 + \nu)!(l - l_1 - m_2 + \nu)!.$$

The summation over the index ν assumes that the arguments of the factorial are positive integers.

The Racah formula can be used to calculate $3j$ symbols but it should be avoided given that symbols up to $l \sim x$ need to be calculated (x is the size parameter). Accurately evaluating a sum of products of factorials quickly becomes an unrealistic task for spheres with large size parameters. Instead, the recursion relations for the $3j$ symbols can be used to generate a table accurately and efficiently [43,44].

Unlike the integral $\mathcal{I}_{l_1 l_2 m_1 l_2 m_2}^A$, the two remaining integrals $\mathcal{I}_{l_1 l_2 m_1 l_2 m_2}^B$ and $\mathcal{I}_{l_1 l_2 m_1 l_2 m_2}^C$ require some additional analysis to resolve.

2. Solution of the second integral

We begin by inserting the definitions from Eq. (9) into Eq. (41) to give

$$\mathcal{I}_{l_1 l_2 m_1 l_2 m_2}^B = \int_0^\pi \sin \theta d\theta \left[\frac{m_1 m_2}{\sin^2 \theta} P_{l_1}^{|m_1|} P_{l_2}^{|m_2|} + \frac{dP_{l_1}^{|m_1|}}{d\theta} \frac{dP_{l_2}^{|m_2|}}{d\theta} \right] P_l^{|m|}.$$

The two associated Legendre functions satisfy the generalized Legendre equation [39]:

$$\frac{1}{\sin \theta} \frac{d}{d\theta} \left(\sin \theta \frac{dP_l^{|m|}}{d\theta} \right) + \left[l(l + 1) - \frac{m^2}{\sin^2 \theta} \right] P_l^{|m|} = 0. \quad (\text{C13})$$

Therefore, by virtue of Eq. (C13), the following relation holds:

$$\frac{1}{\sin \theta} \left[P_{l_2}^{|m_2|} \frac{d}{d\theta} \left(\sin \theta \frac{P_{l_1}^{|m_1|}}{d\theta} \right) + P_{l_1}^{|m_1|} \frac{d}{d\theta} \left(\sin \theta \frac{P_{l_2}^{|m_2|}}{d\theta} \right) \right] + \left[l_1(l_1 + 1) + l_2(l_2 + 1) - \frac{m_1^2 + m_2^2}{\sin^2 \theta} \right] P_{l_1}^{|m_1|} P_{l_2}^{|m_2|} = 0.$$

By reversing the product rule and completing the square, we find after a bit of algebra that

$$\begin{aligned} & \sin \theta \left(\frac{m_1 m_2}{\sin^2 \theta} P_{l_1}^{|m_1|} P_{l_2}^{|m_2|} + \frac{dP_{l_1}^{|m_1|}}{d\theta} \frac{dP_{l_2}^{|m_2|}}{d\theta} \right) \\ &= \frac{1}{2} \frac{d}{d\theta} \left[\sin \theta \frac{d}{d\theta} (P_{l_1}^{|m_1|} P_{l_2}^{|m_2|}) \right] + \frac{1}{2} \left[l_1(l_1 + 1) + l_2(l_2 + 1) - \frac{(m_1 - m_2)^2}{\sin^2 \theta} \right] P_{l_1}^{|m_1|} P_{l_2}^{|m_2|} \sin \theta. \end{aligned} \quad (\text{C14})$$

The integral of the first term on the right-hand side (RHS) of Eq. (C14) is

$$\frac{1}{2} \int_0^\pi d\theta \frac{d}{d\theta} \left[\sin \theta \frac{d}{d\theta} (P_{l_1}^{|m_1|} P_{l_2}^{|m_2|}) \right] P_l^{|m|},$$

which can be integrated by parts twice to give

$$\frac{1}{2} \int_0^\pi d\theta \left[\frac{d}{d\theta} \left(\sin \theta \frac{dP_{l_3}^{|m_3|}}{d\theta} \right) \right] P_{l_1}^{|m_1|} P_{l_2}^{|m_2|}.$$

The term in brackets satisfies Eq. (C13) such that we can make the substitution

$$-\frac{1}{2} \int_0^\pi \sin \theta d\theta \left[l(l + 1) - \frac{m^2}{\sin^2 \theta} \right] P_{l_1}^{|m_1|} P_{l_2}^{|m_2|} P_l^{|m|}.$$

The integral of the second term on the RHS of Eq. (C14) is

$$\frac{1}{2} \int_0^\pi \sin \theta d\theta \left[l_1(l_1 + 1) + l_2(l_2 + 1) - \frac{(m_1 - m_2)^2}{\sin^2 \theta} \right] P_{l_1}^{|m_1|} P_{l_2}^{|m_2|} P_l^{|m|}.$$

Because $m_1 - m_2 = m$, the RHS of Eq. (41) is

$$\int_0^\pi \sin \theta d\theta [m_1 m_2 \pi_{l_1}^{|m_1|} \pi_{l_2}^{|m_2|} + \tau_{l_1}^{|m_1|} \tau_{l_2}^{|m_2|}] P_l^{|m|} = \frac{1}{2} [l_1(l_1 + 1) + l_2(l_2 + 1) - l(l + 1)] \int_0^\pi \sin \theta d\theta P_{l_1}^{|m_1|} P_{l_2}^{|m_2|} P_l^{|m|},$$

which we rewrite as

$$\mathcal{I}_{l_1 l_2 m_1 m_2 l m}^B = \frac{1}{2} [l_1(l_1 + 1) + l_2(l_2 + 1) - l(l + 1)] \mathcal{I}_{l_1 l_2 m_1 m_2 l m}^A, \quad (\text{C15})$$

where the integral $\mathcal{I}_{l_1 l_2 m_1 m_2 l m}^A$ is known from Eq. (C10).

3. Solution of the third integral

In practice, we are faced with two integrals of the form

$$-\int_0^\pi \sin \theta d\theta \pi_{l_1}^{|m_1|} \tau_{l_2}^{|m_2|} P_l^{|m|} = \int_{-1}^1 dz P_{l_1}^{|m_1|} \frac{d}{dz} (P_{l_2}^{|m_2|}) P_l^{|m|}. \quad (\text{C16})$$

Here, we use the fact that the product of two associated Legendre functions can be expressed as a sum over a single associated Legendre function by the use of the expansion [59]

$$P_{l_1}^{m_1} P_l^m = (-1)^{m_1} \sqrt{\frac{(l_1 + m_1)! (l + m)!}{(l_1 - m_1)! (l - m)!}} \sum_{l_i} G_i \sqrt{\frac{(l_i - m_2)!}{(l_i + m_2)!}} P_{l_i}^{m_2}, \quad (\text{C17})$$

where the term G_i is

$$G_i = (2l_i + 1) \begin{pmatrix} l_1 & l_i & l \\ 0 & 0 & 0 \end{pmatrix} \begin{pmatrix} l_1 & l_i & l \\ m_1 & -m_2 & -m \end{pmatrix}. \quad (\text{C18})$$

It is nonzero provided that (1) $|l_1 - l| \leq l_i \leq l_1 + l$, (2) $l_i \geq |m_2|$, and (3) $l_i + l_1 + l$ are even.

We combine this series expansion with the following result [60]

$$\mathcal{I}_{l_2 m_2}^D = \int_{-1}^1 dz \frac{d}{dz} (P_{l_2}^{|m_2|}) P_{l_i}^{|m_2|} = \delta_{0, m_2} - \frac{(l_2 + |m_2|)!}{(l_2 - |m_2|)!} \delta_{2p+1, l_i - l_2} + \frac{(l_i + |m_2|)!}{(l_i - |m_2|)!} \delta_{2p+1, l_2 - l_i}, \quad (\text{C19})$$

with $p = 0, 1, 2, \dots$ being zero or any real positive integers. Then in principle,

$$\mathcal{I}_{l_2 m_2 l m}^C = (-1)^\Lambda \sqrt{\frac{(l_1 + |m_1|)! (l_2 + |m_2|)! (l + |m|)!}{(l_1 - |m_1|)! (l_2 - |m_2|)! (l - |m|)!}} \times \left(m_1 \sum_{l_i=|l_1-l|}^{l_1+l} G_i \sqrt{\frac{(l_2 - |m_2|)! (l_i - |m_2|)!}{(l_2 + |m_2|)! (l_i + |m_2|)!}} \mathcal{I}_{l_2 m_2}^D + m_2 \sum_{l_j=|l_2-l|}^{l_2+l} H_j \sqrt{\frac{(l_j - |m_1|)! (l_1 - |m_1|)!}{(l_j + |m_1|)! (l_1 + |m_1|)!}} \mathcal{I}_{l_1 m_1}^D \right), \quad (\text{C20})$$

where H_j is

$$H_j = (2l_j + 1) \begin{pmatrix} l_j & l_2 & l \\ 0 & 0 & 0 \end{pmatrix} \begin{pmatrix} l_j & l_2 & l \\ m_1 & -m_2 & -m \end{pmatrix}, \quad (\text{C21})$$

and is nonzero provided that (1) $|l_2 - l| \leq l_j \leq l_2 + l$, (2) $l_j \geq |m_1|$, and (3) $l_j + l_2 + l$ are even. A remarkable property of Eq. (C20) is that it is nonzero provided that $l_1 + l_2 + l_3$ is odd. Moreover, it was found numerically that Eq. (C20) vanishes unless the triangle equality $|l_1 - l_2| \leq l \leq l_1 + l_2$ is satisfied. In comparison, Eq. (C15) is nonzero when $l_1 + l_2 + l_3$ is even and when it also satisfies the same triangle equality. This fact is useful when tabulating the integrals, as the infinite summations in Eqs. (32) and (33) become bounded in l_1 and l_2 by the triangle equality and only the integrals that satisfy their respective parity property need to be considered.

APPENDIX D: NET FORCE ON A SPHERICAL PARTICLE

The net radiation force acting on the particle can be calculated by considering the conservation of momentum for the combined system of the electromagnetic field and the particle. The desired result can be obtained by integrating the time-averaged Maxwell stress tensor in the far field [61]

$$\mathbf{F}_{\text{rad}} = r^2 \int_0^{2\pi} \int_0^\pi \langle \hat{\mathbf{e}}_r \cdot \vec{T} \rangle \sin \theta d\theta d\phi. \quad (\text{D1})$$

The z component of the radiation force is found by projecting \mathbf{F}_{rad} onto the z axis

$$F_z = r^2 \int_0^{2\pi} \int_0^\pi \hat{\mathbf{e}}_z \cdot \langle \hat{\mathbf{e}}_r \cdot \vec{T} \rangle \sin \theta d\theta d\phi. \quad (\text{D2})$$

However, in our application and ignoring absorption, it is more straightforward to express the radiation pressure force on each layer:

$$\begin{aligned} F_z^{(j)} &= a_j^2 \int_0^{2\pi} \int_0^\pi \hat{\mathbf{e}}_z \cdot \left(\langle \hat{\mathbf{e}}_r \cdot \vec{T} \rangle_{r=a_j^+} - \langle \hat{\mathbf{e}}_r \cdot \vec{T} \rangle_{r=a_j^-} \right) \sin \theta d\theta d\phi \\ &= a_j^2 \int_0^{2\pi} \int_0^\pi \sigma_j(\theta, \phi) \cos \theta \sin \theta d\theta d\phi. \end{aligned} \quad (\text{D3})$$

This is because the net force acting at the interface of each layer is

$$F_z^{(j)} = \frac{4}{3} \pi a_j^2 \sigma_1^{(j)}, \quad (\text{D4})$$

with $\sigma_1^{(j)}$ denoting the coefficient of the first harmonic $Y_{1,0}$ on the j th layer. The net force acting on the particle is found by

summing each contributing layer

$$F_z = \frac{4}{3} \pi \sum_j a_j^2 \sigma_1^{(j)}. \quad (\text{D5})$$

It can be shown that the method of calculating the net force from Eq. (D5) is equivalent to Eq. (D2) provided that absorption is absent. To start off, we insert the spherical harmonic expansion from Eq. (27) into Eq. (D3) to yield

$$\begin{aligned} F_z^{(j)} &= a_j^2 \int_0^{2\pi} \int_0^\pi \sum_{l=1}^\infty \sum_{m=-l}^l \sigma_{lm}^{(j)} \\ &\quad \times Y_{lm}(\theta, \phi) \cos \theta \sin \theta d\theta d\phi \\ &= a_j^2 \sum_{l=1}^\infty \sum_{m=-l}^l \sigma_{lm}^{(j)} \int_0^{2\pi} e^{im\phi} d\phi \\ &\quad \times \int_0^\pi \sin \theta d\theta P_l^m(\cos \theta) \cos \theta. \end{aligned} \quad (\text{D6})$$

The azimuthal integral results in $2\pi \delta_{m,0}$ and so $\sigma_{l,m}^{(j)} \rightarrow \sigma_l^{(j)}$

$$F_z^{(j)} = 2\pi a_j^2 \sum_{l=1}^\infty \sigma_l^{(j)} \int_0^\pi \sin \theta d\theta P_l(\cos \theta) \cos \theta. \quad (\text{D7})$$

Recognizing that $\cos \theta = P_1(\cos \theta)$, we make use of the orthogonality of Legendre polynomials

$$\int_0^\pi \sin \theta d\theta P_l P_1 = \frac{2}{2l+1} \delta_{l,1} = \frac{2}{3} \delta_{l,1}, \quad (\text{D8})$$

to yield the net force in the z direction on the j th layer [Eq. (D4)].

- [1] A. Ashkin and J. M. Dziedzic, Radiation Pressure on a Free Liquid Surface, *Phys. Rev. Lett.* **30**, 139 (1973).
 [2] J. P. Gordon, Radiation forces and momenta in dielectric media, *Phys. Rev. A* **8**, 14 (1973).

- [3] F. Robinson, Electromagnetic stress and momentum in matter, *Phys. Rep.* **16**, 313 (1975).
 [4] H.-M. Lai and K. Young, Response of a liquid surface to the passage of an intense laser pulse, *Phys. Rev. A* **14**, 2329 (1976).

- [5] J. Z. Zhang and R. K. Chang, Shape distortion of a single water droplet by laser-induced electrostriction, *Opt. Lett.* **13**, 916 (1988).
- [6] H. M. Lai, P. T. Leung, K. L. Poon, and K. Young, Electrostrictive distortion of a micrometer-sized droplet by a laser pulse, *J. Opt. Soc. Am. B* **6**, 2430 (1989).
- [7] I. Brevik and R. Kluge, Oscillations of a water droplet illuminated by a linearly polarized laser pulse, *J. Opt. Soc. Am. B* **16**, 976 (1999).
- [8] S. Å. Ellingsen, Theory of microdroplet and microbubble deformation by Gaussian laser beam, *J. Opt. Soc. Am. B* **30**, 1694 (2013).
- [9] P. Zhang, S. Jung, A. Lee, and Y. Xu, Radiation-pressure-induced nonlinearity in microdroplets, *Phys. Rev. E* **92**, 063033 (2015).
- [10] A. Ashkin, Acceleration and Trapping of Particles by Radiation Pressure, *Phys. Rev. Lett.* **24**, 156 (1970).
- [11] A. Ashkin and J. M. Dziedzic, Optical levitation by radiation pressure, *Appl. Phys. Lett.* **19**, 283 (1971).
- [12] A. Ashkin, J. M. Dziedzic, J. E. Bjorkholm, and S. Chu, Observation of a single-beam gradient force optical trap for dielectric particles, *Opt. Lett.* **11**, 288 (1986).
- [13] J. E. Curtis, B. A. Koss, and D. G. Grier, Dynamic holographic optical tweezers, *Opt. Commun.* **207**, 169 (2002).
- [14] R. J. Hopkins, L. Mitchem, A. D. Ward, and J. P. Reid, Control and characterisation of a single aerosol droplet in a single-beam gradient-force optical trap, *Phys. Chem. Chem. Phys.* **6**, 4924 (2004).
- [15] J. Chen, J. Ng, Z. Lin, and C. T. Chan, Optical pulling force, *Nat. Photon.* **5**, 531 (2011).
- [16] A. Jonáš and P. Zemanek, Light at work: The use of optical forces for particle manipulation, sorting, and analysis, *Electrophoresis* **29**, 4813 (2008).
- [17] K. C. Neuman and A. Nagy, Single-molecule force spectroscopy: Optical tweezers, magnetic tweezers, and atomic force microscopy, *Nat. Methods* **5**, 491 (2008).
- [18] A. Rafferty, K. Gorkowski, A. Zuend, and T. C. Preston, Optical deformation of single aerosol particles, *Proc. Natl. Acad. Sci. USA* **116**, 19880 (2019).
- [19] G. Bolognesi, A. Hargreaves, A. D. Ward, A. K. Kirby, C. D. Bain, and O. Ces, Microfluidic generation of monodisperse ultra-low interfacial tension oil droplets in water, *RSC Adv.* **5**, 8114 (2015).
- [20] A. D. Ward, M. G. Berry, C. D. Mellor, and C. D. Bain, Optical sculpture: Controlled deformation of emulsion droplets with ultralow interfacial tensions using optical tweezers, *Chem. Commun.* **206**, 4515 (2006).
- [21] D. Tapp, J. M. Taylor, A. S. Lubansky, C. D. Bain, and B. Chakrabarti, Theoretical analysis for the optical deformation of emulsion droplets, *Opt. Express* **22**, 4523 (2014).
- [22] J. Guck, R. Ananthakrishnan, T. J. Moon, C. C. Cunningham, and J. Käs, Optical Deformability of Soft Biological Dielectrics, *Phys. Rev. Lett.* **84**, 5451 (2000).
- [23] J. Guck, R. Ananthakrishnan, H. Mahmood, T. J. Moon, C. C. Cunningham, and J. Käs, The optical stretcher: A novel laser tool to micromanipulate cells, *Biophys. J.* **81**, 767 (2001).
- [24] H. Köhler, The nucleus in and the growth of hygroscopic droplets, *Trans. Faraday Soc.* **32**, 1152 (1936).
- [25] C. R. Ruehl, J. F. Davies, and K. R. Wilson, An interfacial mechanism for cloud droplet formation on organic aerosols, *Science* **351**, 1447 (2016).
- [26] J. Ovadnevaite, A. Zuend, A. Laaksonen, K. J. Sanchez, G. Roberts, D. Ceburnis, S. Decesari, M. Rinaldi, N. Hodas, M. C. Facchini *et al.* Surface tension prevails over solute effect in organic-influenced cloud droplet activation, *Nature (London)* **546**, 637 (2017).
- [27] J. F. Davies, A. Zuend, and K. R. Wilson, Technical note: The role of evolving surface tension in the formation of cloud droplets, *Atmos. Chem. Phys.* **19**, 2933 (2019).
- [28] A. K. Bertram, S. T. Martin, S. J. Hanna, M. L. Smith, A. Bodsworth, Q. Chen, M. Kuwata, A. Liu, Y. You, and S. R. Zorn, Predicting the relative humidities of liquid-liquid phase separation, efflorescence, and deliquescence of mixed particles of ammonium sulfate, organic material, and water using the organic-to-sulfate mass ratio of the particle and the oxygen-to-carbon elemental ratio of the organic component, *Atmos. Chem. Phys.* **11**, 10995 (2011).
- [29] R. E. O'Brien, B. Wang, S. T. Kelly, N. Lundt, Y. You, A. K. Bertram, S. R. Leone, A. Laskin, and M. K. Gilles, Liquid-liquid phase separation in aerosol particles: Imaging at the nanometer scale, *Environ. Sci. Technol.* **49**, 4995 (2015).
- [30] M. A. Freedman, Phase separation in organic aerosol, *Chem. Soc. Rev.* **46**, 7694 (2017).
- [31] N. B. Vargaftik, B. N. Volkov, and L. D. Voljak, International tables of the surface tension of water, *J. Phys. Chem. Ref. Data* **12**, 817 (1983).
- [32] H. M. Lai, P. T. Leung, K. Young, P. W. Barber, and S. C. Hill, Time-independent perturbation for leaking electromagnetic modes in open systems with application to resonances in microdroplets, *Phys. Rev. A* **41**, 5187 (1990).
- [33] H. M. Lai, C. C. Lam, P. T. Leung, and K. Young, Effect of perturbations on the widths of narrow morphology-dependent resonances in Mie scattering, *J. Opt. Soc. Am. B* **8**, 1962 (1991).
- [34] A. J. Trevitt, P. J. Wearne, E. J. Bieske, and M. D. Schuder, Observation of nondegenerate cavity modes for a distorted polystyrene microsphere, *Opt. Lett.* **31**, 2211 (2006).
- [35] A. J. Trevitt, P. J. Wearne, and E. J. Bieske, Coalescence of levitated polystyrene microspheres, *J. Aerosol Sci.* **40**, 431 (2009).
- [36] S. C. Yorulmaz, M. Mestre, M. Muradoglu, B. E. Alaca, and A. Kiraz, Controlled observation of nondegenerate cavity modes in a microdroplet on a superhydrophobic surface, *Opt. Commun.* **282**, 3024 (2009).
- [37] I. Brevik, Experiments in phenomenological electrostatics and the electromagnetic energy-momentum tensor, *Phys. Rep.* **52**, 133 (1979).
- [38] J. P. Barton, D. R. Alexander, and S. A. Schaub, Theoretical determination of net radiation force and torque for a spherical particle illuminated by a focused laser beam, *J. Appl. Phys.* **66**, 4594 (1989).
- [39] C. F. Bohren and D. R. Huffman, *Absorption and Scattering of Light by Small Particles* (Wiley-VCH, Berlin, 1983).
- [40] J. A. Lock, Improved Gaussian beam-scattering algorithm, *Appl. Opt.* **34**, 559 (1995).
- [41] J. Taylor and G. Love, Multipole expansion of Bessel and Gaussian beams for Mie scattering calculations, *J. Opt. Soc. Am. A* **26**, 278 (2009).

- [42] H. Polaert, G. Grehan, and G. Gouesbet, Forces and torques exerted on a multilayered spherical particle by a focused Gaussian beam, *Opt. Commun.* **155**, 169 (1998).
- [43] K. Schulten and R. G. Gordon, Exact recursive evaluation of $3j$ and $6j$ coefficients for quantum mechanical coupling of angular momenta, *J. Math. Phys.* **16**, 1961 (1975).
- [44] J. H. Luscombe and M. Luban, Simplified recursive algorithm for Wigner $3j$ and $6j$ symbols, *Phys. Rev. E* **57**, 7274 (1998).
- [45] M. Daimon and A. Masumura, Measurement of the refractive index of distilled water from the near-infrared region to the ultraviolet region, *Appl. Opt.* **46**, 3811 (2007).
- [46] N.-O. A. Kwamena, J. Buajerern, and J. P. Reid, Equilibrium morphology of mixed organic/inorganic/aqueous aerosol droplets: Investigating the effect of relative humidity and surfactants, *J. Phys. Chem.* **114**, 5787 (2010).
- [47] F. Xu, J. A. Lock, G. Gouesbet, and C. Tropea, Optical stress on the surface of a particle: Homogeneous sphere, *Phys. Rev. A* **79**, 053808 (2009).
- [48] J. P. Barton, D. R. Alexander, and S. A. Schaub, Internal fields of a spherical particle illuminated by a tightly focused laser beam: Focal point positioning effects at resonance, *J. Appl. Phys.* **65**, 2900 (1989).
- [49] J. A. Lock, Excitation efficiency of a morphology-dependent resonance by a focused Gaussian beam, *J. Opt. Soc. Am. A* **15**, 2986 (1998).
- [50] W. M. Haynes, D. R. Lide, and T. J. Bruno, *CRC Handbook of Chemistry and Physics: A Ready-Reference Book of Chemical and Physical Data* (CRC Press, Boca Raton, FL, 2013).
- [51] B. Vennes and T. C. Preston, Calculating and fitting morphology-dependent resonances of a spherical particle with a concentric spherical shell, *J. Opt. Soc. Am. A* **36**, 2089 (2019).
- [52] T. Čižmár, V. Kollárová, Z. Bouchal, and P. Zemánek, Sub-micron particle organization by self-imaging of non-diffracting beams, *New J. Phys.* **8**, 43 (2006).
- [53] P. Chýlek and J. Zhan, Interference structure of the Mie extinction cross section, *J. Opt. Soc. Am. A* **6**, 1846 (1989).
- [54] W. R. C. Somerville, B. Auguié, and E. C. Le Ru, SMARTIES: User-friendly codes for fast and accurate calculations of light scattering by spheroids, *J. Quant. Spectrosc. Radiat. Transfer* **174**, 39 (2016).
- [55] T. C. Preston and J. P. Reid, Angular scattering of light by a homogeneous spherical particle in a zeroth-order Bessel beam and its relationship to plane wave scattering, *J. Opt. Soc. Am. A* **32**, 1053 (2015).
- [56] D. W. Mackowski, Calculation of total cross sections of multiple-sphere clusters, *J. Opt. Soc. Am. A* **11**, 2851 (1994).
- [57] S.-H. Dong and R. Lemus, The overlap integral of three associated Legendre polynomials, *Appl. Math. Lett.* **15**, 541 (2002).
- [58] V. Devanathan, *Angular Momentum Techniques in Quantum Mechanics* (Kluwer Academic, Dordrecht, 2002).
- [59] H. Mavromatis and R. Alassar, A generalized formula for the integral of three associated Legendre polynomials, *Appl. Math. Lett.* **12**, 101 (1999).
- [60] S. Sammadar, Some integrals involving associated Legendre functions, *Math. Comput.* **28**, 257 (1974).
- [61] A. A. R. Neves and C. L. Cesar, Analytical calculation of optical forces on spherical particles in optical tweezers: Tutorial, *J. Opt. Soc. Am. B* **36**, 1525 (2019).